Journal Pre-proof



Computational and semiempirical design, and hydrogen storage behavior characterization of non-equiatomic Zr-Ti-Mn-Fe-Mo C14-Laves phase multicomponent alloy

Badr El Aalami, Guillaume Esser, Hosni Idrissi, Yaroslav Filinchuk, Vera Trabadelo

PII: S1385-8947(26)11558-7

DOI: https://doi.org/10.1016/j.cej.2026.184088

Reference: CEJ 184088

To appear in:

Received date: 25 July 2026

Revised date: 15 October 2026

Accepted date: 8 November 2026

Please cite this article as: B. El Aalami, G. Esser, H. Idrissi, et al., Computational and semiempirical design, and hydrogen storage behavior characterization of non-equiatomic Zr-Ti-Mn-Fe-Mo C14-Laves phase multicomponent alloy, (2026), https://doi.org/10.1016/j.cej.2026.184088

This is a PDF of an article that has undergone enhancements after acceptance, such as the addition of a cover page and metadata, and formatting for readability. This version will undergo additional copyediting, typesetting and review before it is published in its final form. As such, this version is no longer the Accepted Manuscript, but it is not yet the definitive Version of Record; we are providing this early version to give early visibility of the article. Please note that Elsevier's sharing policy for the Published Journal Article applies to this version, see: https://www.elsevier.com/about/policies-and-standards/sharing#4-published-journal-article. Please also note that, during the production process, errors may be discovered which could affect the content, and all legal disclaimers that apply to the journal pertain.

© 2026 Published by Elsevier B.V.

Computational and semiempirical design, and hydrogen storage behavior characterization of non-equiatomic Zr-Ti-Mn-Fe-Mo C14-Laves phase multicomponent alloy

Badr El Aalami[ab], Guillaume Esser[c], Hosni Idrissi[b], Yaroslav Filinchuk[c], Vera Trabadelo[a]*

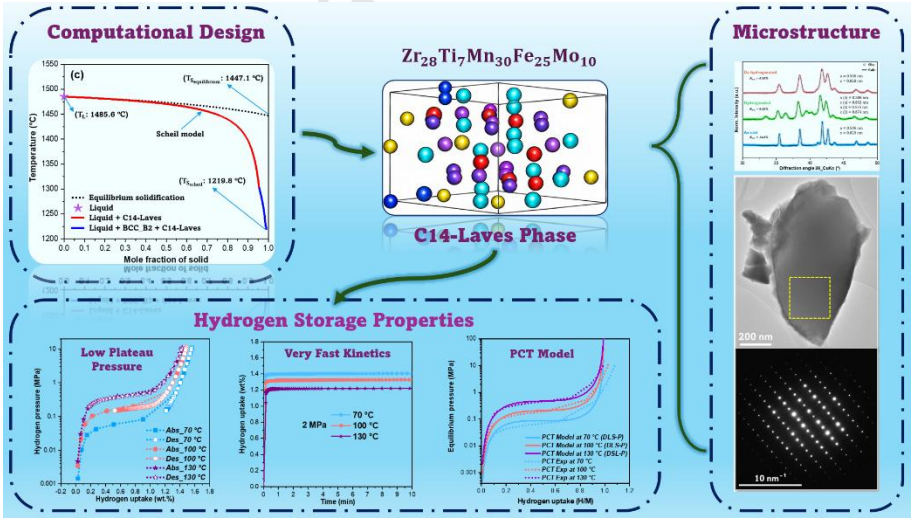
**E-mail: vera.trabadelo@um6p.ma*

[a]*High Throughput Multidisciplinary Research Laboratory (HTMR), College of Chemical Sciences and Engineering (CCSE), Mohammed VI Polytechnic University (UM6P), Lot 660, Hay Moulay Rachid, Benguerir 43150, Morocco*

[b]*Institute of Mechanics, Materials and Civil Engineering, IMAP Division, UCLouvain, Place Sainte Barbe, 2, B-1348, Louvain-la-Neuve, Belgium*

[c]*Institute of Condensed Matter and Nanoscience, UCLouvain, Place L. Pasteur 1, B-1348, Louvain-la-Neuve, Belgium*

Graphical Abstract



Abstract

C14-Laves phase based multicomponent alloys demonstrate significant promise for solid-state hydrogen storage thanks to the vast space of compositional design, easy activation process, and their severe lattice distortion, allowing for rapid kinetics and

absorption of substantial amounts of hydrogen at low to intermediate temperatures. In this paper, the non-equiatomic $Zr_{28}Ti_7Mn_{30}Fe_{25}Mo_{10}$ alloy was rationally designed by combining semiempirical parameters with computational thermodynamic tools such as CALPHAD method and Scheil model. Additionally, pressure-composition-temperature (PCT) diagrams were initially predicted using a thermodynamic model to assess the hydrogen equilibrium pressure of the alloy and subsequently refined based on experimental results to better reproduce the alloy's hydrogen storage behavior. The alloy was prepared via arc melting and structurally crystallized as a single C14-Laves phase structure. Volumetric PCT measurements show a maximum hydrogen capacity of 1.56 wt% ($H/M = 1.08$) at 70 °C under 10 MPa, with equilibrium pressures increasing from 0.07 MPa (70 °C) to 0.46 MPa (130 °C) at $H/M = 0.5$. Contrasting with the sloping behavior predicted by the initial model, the refined model reproduces the experimental PCT diagrams more accurately, capturing a plateau-like region consistent with a mixed absorption mechanism (α–β transition). The alloy exhibits extremely fast kinetics with no incubation time and $\sim 99\%$ uptake within seconds, while absorbing > 0.9 wt% near ambient pressure. Thermodynamic analysis reveals moderate hydride stability ($\Delta H_{Abs} \approx -36\ kJ/mol\ H_2$), enabling reversible storage at moderate temperatures, although full desorption requires $\geq 200\ ℃$. The alloy retains $\geq 94\%$ capacity after seven cycles, with excellent structural stability maintained despite lattice expansion and particle pulverization. Overall, this composition offers a favorable balance between low-pressure operation, fast kinetics, and cycling stability, highlighting its potential for practical hydrogen storage.

Keywords

Solid-state hydrogen storage, High entropy alloys, Multicomponent alloys, C14-Laves phase, CALPHAD, Low-equilibrium pressure, C14-Laves hydride, Kinetics

1. Introduction

In the last decades, societies worldwide have adopted the energy transition from fossil fuels to cleaner and renewable energy sources to provide long-term energy supply and mitigate the temperature rising due to excessive CO_2 emissions.[1] Hydrogen for instance, as an ideal, most abundant element, and clean energy carrier,

can play a crucial role in the global energy transition by converting efficiently the surplus energy of solar and wind energy sources to green hydrogen via the electrolysis of water, allowing for effective flexibility and reliability of using renewable energies.[2,3] However, the main challenge in making the hydrogen technology efficient and cost-effective at large scale is the need for safe and compact storage systems.[4,5] Among various hydrogen storage methods, solid-state storage through chemisorption in metal hydrides (MHs) is considered safer and provides higher energy density, low overall cost, and good reversibility under very low-operating pressures compared to gaseous and liquid systems.[6,7]

MHs have been widely studied, beginning with MgH_2 as the most popular hydride system, followed by the development of binary and ternary hydrides, and eventually to more complex hydride materials. By storing hydrogen in their lattice interstitial sites, these MHs offer compact solid-state hydrogen storage systems for both stationary and onboard applications and even beyond, including hydrogen compression, hydrogen fuel cells, electrochemical energy storage (e.g.; $Ni-MH$ batteries), hydrogen purification systems, and hydrogen transport.[8] The key factor that governs the performance of these applications is the chemical composition of the MHs.[9] In this context, high-entropy alloys (HEAs) or multicomponent alloys with intermetallic structures have gained extensive interests for hydrogen storage applications.[10] These intermetallic alloys are typically made-up of a combination of a hydride-forming elements (A-type) and a non-hydride forming elements (B-type), resulting in unique crystal structures known as Laves phase compounds that are commonly classified into: C14 (Hexagonal $MgZn_2-type$), C15 (Cubic $MgCu_2-type$), and C36 (Hexagonal $MgNi_2-type$).[11] The C14-Laves phase intermetallics with typical AB_2 (i.e.; $ZrMn_2$, $ZrCr_2$) stoichiometry are the most studied for hydrogen storage owing to their higher hydrogen capacity and the advantage of operating at lower hydrogen pressures compared to AB and AB_5 compounds.[12,13,14]

The formation and stability of the C14-Laves phase can be effectively predicted using thermodynamic computational tools such as the CALPHAD method and the Scheil solidification model.[15] The high number of constituent elements provides vast compositional flexibility to further tailor the hydrogen storage properties.[16] Although body-centered cubic (BCC) HEAs and Mg-based alloys exhibit relatively high gravimetric capacities, their high activation barriers, poor kinetics, and unfavorable

thermodynamic properties are the main limitations for their large-scale commercialization.[17] In contrast, C14-Laves HEAs may show modest hydrogen storage capacities but the operating conditions matter far more than the absolute capacities. Near-ambient pressure offers simultaneously, better safety, minimum compression energy requirements, lower cost, and simplicity.[13] However, in some cases a very low equilibrium pressure, particularly below atmospheric pressure, can affect negatively the hydrogen desorption process.[18,19] In such cases, a moderate amount of heat is necessary to shift up the equilibrium pressure and enable complete dehydrogenation of the hydride.

Numerous studies on C14-Laves multicomponent alloys have demonstrated the effect of moderate temperatures on the hydrogen storage performance. Aranda et al.[20] showed that increasing the temperature from room temperature to moderate values (i.e.; 50, 100, 150, and 200 °C) reduces the maximum hydrogen uptake whereas increasing the equilibrium pressure. Similar trends have been consistently reported in comparable works.[15,21,22] Nevertheless, increasing the temperature can significantly improve hydrogen reversibility. Ponsoni et al.[21] showed that while their $(\mathrm{Ti}_{0.5}\mathrm{Zr}_{0.5})_1(\mathrm{Mn}_{0.5}\mathrm{Cr}_{0.5})_2$ alloy exhibited incomplete desorption at 30 °C, full hydrogen release was achieved at 90 °C. Moreover, moderate thermal conditions reduce hysteresis by facilitating atomic mobility and promoting strain relaxation.[22,23] Furthermore, it has been revealed that hydrogen storage properties can be considerably enhanced by controlling some semiempirical parameters such as atomic size mismatch (δ) and valence electron concentration (VEC).[24] Ma et al.[25] reported that the incorporation of multiple elements with different atomic sizes increases the size mismatch, leading to severe lattice distortion and the generation of crystal defects. Such lattice imperfections are the main factors responsible for the rapid hydrogen absorption kinetics and enhanced hydrogen capacity at low temperatures. Edalati et al.[26] investigated the hydrogen behavior of the TiZrCrMnFeNi multicomponent alloy having a single C14-Laves phase with a VEC of exactly 6.4. They concluded that under these conditions, the alloy was able to reversibly absorb and desorb up to 1.70 wt% of hydrogen at room temperature, highlighting the significant role of preliminary alloy composition design. Additionally, Zr-based AB_2 C14-Laves HEAs have shown increased hydrogen uptake with the increase of Zr content, indicating the critical impact of Zr in improving hydrogen storage properties. Andrade et al.[27] studied the hydrogen storage performance of

alloys in the Zr-Cr-Mn-Fe-Ni system and found that the alloy with higher Zr content achieved an increased capacity of 1.80 wt%. In addition, Zr plays an essential role in the stabilization of the C14-Laves phase and reducing the equilibrium plateau-pressure due to its high affinity to hydrogen. However, in certain cases, a high concentration of Zr may induce incomplete release of hydrogen, likely due to the strong Zr-H bonding.[28]

Building on insights from earlier studies, efforts have been directed toward improving the design of HEAs prior to synthesis. Many strategies can be adopted to design properly C14-Laves phase alloys for hydrogen storage applications. Ponsoni et al.[16] have constructed a systematic approach for alloy design, starting by computing relevant semiempirical parameters to assess the feasibility of forming a C14-Laves phase, and subsequently evaluating phase stability through the CALPHAD method. Marques et al.[15] employed the thermodynamic computation of the solidification path under non-equilibrium conditions using the Scheil model to further predict the stability of the C14-Laves phase and possible elemental segregation. In addition, a thermodynamic model for predicting the pressure-composition-temperature (PCT) isotherms of C14-Laves phase during solid-solution hydrogenation is also developed in the work of Ponsoni et al.[16] Furthermore, Marques et al.[15] refined the model to enhance its agreement with experimental PCT diagrams, enabling the exploration of different alloy compositions and stoichiometries and the prediction of equilibrium plateau pressures at moderate temperatures. Consequently, this predictive approach has been widely adopted in recent works focused on designing C14-Laves alloys for hydrogen storage applications.[15,21,22]

The present work demonstrates a rational design approach by developing a non-equiatomic multicomponent alloy based on the Zr-Ti-Mn-Fe-Mo system that can crystallize majorly as single C14-Laves phase and absorb hydrogen under moderate temperature-pressure operating conditions. The study focuses on the experimental validation the selected composition in terms of its microstructure and hydrogen storage behavior, providing a proof of concept for the proposed design strategy. The calculated PCT diagrams were initially predicted using a thermodynamic model to assess the hydrogen equilibrium pressure of the alloy as a function of temperature and subsequently refined based on experimental results to better reproduce the alloy's hydrogen storage behavior. The selected

composition,– $Zr_{28}Ti_7Mn_{30}Fe_{25}Mo_{10}$ –, was prepared via arc melting and was experimentally investigated in terms of phase composition, microstructure, absorption/desorption PCT isotherms, chemisorption kinetics, and cycling stability. The thermodynamics of the hydrogenation and the effect of moderate heating on the hydrogen storage performance were evaluated, as the designed alloy exhibits a stable C14-Laves structure, distinguishing it from previous reported compositions by its rapid absorption kinetics and low thermodynamic plateau-pressure.

2. Experimental Details

2.1. Alloy Fabrication

The $Zr_{28}Ti_7Mn_{30}Fe_{25}Mo_{10}$ alloy was produced via arc melting technique. The raw materials used in this work were high-purity Zr (99.98%), Ti (99.995%), Mn (99.95%), Fe (≥ 99.99%), and Mo (≥ 99.9%) foils and chips. They were purchased from commercial suppliers (Goodfellow and Merck) and utilized as-received without additional purification. The melting process was achieved in an electric arc melting furnace (Arc 50 Melter from Arcast INC) under the protection of high-purity argon atmosphere (99.999%) using a non-consumable electrode of tungsten and a water-cooled copper crucible. The metals were loaded inside the crucible in an ordered way according to their melting point. Elements with higher melting temperature (Mo and Zr) were put on top while the other elements (Ti, Fe, and Mn) with lower melting temperature were placed on the bottom. Due to its low melting point, an excess amount of Mn (5 to 7 wt%) was added to compensate for Mn evaporation. To achieve compositional homogeneity, the mixture was flipped and remelted four times and a Ti getter was melted each time prior to the alloy to reduce any residual oxygen remaining in the chamber. After arc melting, the as-cast ingot, which weighs approximately 10 g, was subsequently polished to remove grease and any surface oxides before being crushed and investigated by several techniques. A summary of the synthesis process of the $Zr_{28}Ti_7Mn_{30}Fe_{25}Mo_{10}$ alloy is given in **Scheme 1**.

2.2. Structural and Microstructural Characterization

First, the as-cast alloy sample was hand crushed into powder in open air using a mortar and pestle. The chemical composition of the obtained particles was determined by inductively coupled plasma optical emission spectrometry (ICP-OES) analysis using the Agilent 5100 spectrometer. The crystalline structure of the alloy

was characterized via X-ray diffraction (XRD) measurements using a Bruker D8 Advance diffractometer with $\mathrm{Cu}-\mathrm{K}_{\alpha}$ radiation source ($\lambda = 1.5406\,\text{Å}$) operating at 40 kV and 40 mA conditions. The XRD data were acquired in the 2θ scanning range of 20 and 100° with a step of 0.02°. To determine the lattice parameters, the Rietveld refinement method was used to refine the XRD profiles via FullProf software.

The microstructural analysis was conducted by scanning electron microscopy (SEM) and transmission electron microscopy (TEM). For SEM analysis, a bulk sample of the alloy powder was carefully embedded in conductive resin, mechanically ground using successive sandpapers, and then finely polished using diamond suspensions with different particle size. To reveal the microstructural features of the alloy, the polished sample was chemically etched using HF solution for 10 seconds. The morphology of the polished particles was observed by a Zeiss Ultra 55 FEG SEM equipped with energy dispersive X-ray spectroscopy (EDS, BRUKER Detector) for the elemental distribution analysis. For nanoscale structure investigations, around 40 mg of the crushed sample was dispersed in ethanol and ultrasonicated for 20 min. With the help of a micropipette, three drops of the suspension were deposited onto a copper grid coated with an amorphous thin carbon film and directly examined by a Thermofisher Talos F200i TEM operating at 200 kV.

2.3. Hydrogen Storage Characterization

The hydrogen storage performance of the alloy was evaluated by an IMI-HTP Sievert's apparatus from Hiden Isochema and was used to perform the volumetric gas sorption experiments. About 1.3 g of the powdered sample was loaded into a stainless steel sample cell and covered with roughly 0.02 cm^3 of quartz wool (Thermal Ceramics, Ceramic Fiber type 520) to secure the sample into the pre-weighed reactor. First, the sample was pre-heated and degassed under a dynamic vacuum at 200 °C (with a heating rate of 10 °C/min) for at least 2 h, then activated upon one 10 MPa hydrogen absorption/desorption cycle at 130 °C before any hydrogenation test. Subsequently the pressure-composition-temperature isotherms (PCT) along with kinetics were measured at 130, 100, and 70 °C respectively. In addition, hydrogenation/dehydrogenation cycles were conducted for 7 iterations under 10 MPa at 130, 100, and 70 °C.

Structural examination of the hydrogenated sample was carried out using XRD and SEM analysis. XRD analysis was conducted using a MAR345 diffractometer with X-

rays generated by an Incoatec Microfocus Source HIGHBRILLIANCE (IμS HIGHBRILLIANCE) Mo ELM47 operating at 50 kV and 1000 μA ($\lambda = 0.71073\,\text{Å}$). The hydrogenated sample was loaded in a glass capillary (0.7 mm, Hilgenberg GmbH) immediately after removal from the reactor of the Sievert's equipment, and diffraction data were integrated using the Fit2D software (a 0.1 mm diameter capillary filled with LaB_6 was used as a calibrant).

To investigate the desorption behavior of the hydrogenated sample, differential scanning calorimetry (DSC) and thermogravimetric analysis (TGA) measurements were conducted on roughly 8 mg of hydrogenated sample inside an Al_2O_3 crucible from room temperature to 600 °C at a heating rate of 5 °C/min using a Netzsch STA 449 F3 Jupiter thermal analyzer. The DSC and TGA measurements were carried out under the protection of an inert environment of argon gas (50 mL/min) to prevent any oxidation of the hydrogenated samples.

3. Results and Discussion

The alloy's chemical composition within the quinary ZrTiMnFeMo system was designed to obtain a single-phase system, allowing for a direct evaluation of its intrinsic hydrogen storage properties. The hydrogen storage performance of the $Zr_{28}Ti_7Mn_{30}Fe_{25}Mo_{10}$ alloy, including hydrogen capacity, absorption kinetics, and cycling stability, were investigated at moderate temperatures (70, 100, and 130 °C). This is particularly relevant for practical operation conditions that are compatible with low-grade heat sources and enhanced system safety.

3.1. Composition Design, Phase Formation, and Thermodynamic Modeling

The alloying elements were initially selected and categorized according to their affinity towards hydrogen into two types: A-type (Zr, Ti) as hydride forming elements and B-type (Mn, Fe, Mo) as non-hydride forming elements. The number and concentrations of these elements were chosen with respect to the classical definition of HEAs, requiring at least five principal elements, each with a concentration between 5 and 35 at%.[29,30] **Table S1** (Supporting Information) summarizes the basic physical properties of these elements. The non-equiatomic $Zr_{28}Ti_7Mn_{30}Fe_{25}Mo_{10}$ multi-principal element alloy was designed based on the combination of the semiempirical parameters calculation approach and the CALPHAD method. Subsequently, the non-equilibrium solidification behavior and segregation tendency during cooling in the

present alloy were assessed via the Scheil-Gulliver model. Finally, a thermodynamic model for predicting the PCT isotherms as well as the thermodynamic equilibrium pressures of the alloy will be shown. An overall discussion is then provided to correlate the results and highlight the implications for the alloy design.

3.1.1. Semiempirical Parameters

The phase formation is fundamentally linked to the alloying elements. Therefore, the computation of some key semiempirical parameters at a first place is considered as an important step for the phase selection.[16,31] These parameters are classified as geometrical factors such as atomic size mismatch (δ) and atomic size ratio (r_A/r_B), electronic factors including valence electron concentration (VEC) and electronegativity difference ($\Delta^{\chi}_{\mathrm{Allen}}$), and thermodynamic factors such as mixing entropy (ΔS_{mix}) and mixing enthalpy (ΔH_{mix}). To verify the likelihood to form the C14-Laves phase within the selected composition, the above semiempirical parameters were systematically calculated via the equations reported in **S2** (Supporting Information), and have been employed under defined restrictions.[16,31] **Table S2** (Supporting Information) shows the obtained values of ΔS_{mix}, ΔH_{mix}, VEC, δ, r_A/r_B, and $\Delta^{\chi}_{\mathrm{Allen}}$.

The calculated value of the mixing entropy (ΔS_{mix}) is equal to 12.31 J/(mol.K). This value is slightly lower than the entropy threshold ($\Delta S_{\mathrm{mix}} > 1.5R = 12.47$ J/(mol.K)) for HEAs, which places the $Zr_{28}Ti_7Mn_{30}Fe_{25}Mo_{10}$ alloy in the medium entropy alloy (MEA) category.[29] A higher value of mixing entropy promotes the stability of a random solid-solution (a fully disordered alloy). However, C14-laves phase alloys are typically partly ordered AB_2 compounds with two distinct sublattices; A-type (large atoms) and B-type (small atoms).[16] Therefore, this ordering causes the mixing entropy of the resulting phase to reduce. Nonetheless, such value of ΔS_{mix}, 12.31 J/(mol.K), still falls in the range of random solid-solution formation, $11 \leq \Delta S_{\mathrm{mix}} \leq 19.5$ J/(K·mol), given by Guo et al.[32] For the enthalpic contribution, C14-Laves phases alloys can form within the mixing enthalpy range of -22 to 7 kJ/mol.[32,33] In the investigated composition, the calculated ΔH_{mix} is equal to -14.16 kJ/mol, which is within the defined range. Moreover, this value is moderately negative which suggests that the present C14-Laves phase alloy is enthalpically stabilized.[24] It should be noted that the value of the ΔH_{mix} here, mainly results from the higher contribution of the mixing enthalpies -6.95 and -5.11 kJ/mol of the two pairs Zr-Fe and Zr-Mn, respectively,[34] as

the concentration of these elements is quite large in the $Zr_{28}Ti_7Mn_{30}Fe_{25}Mo_{10}$ alloy. The rest of the contributions of the other pairs is very small due to the low atomic fractions of Mo and Ti as represented in **Table S1** (Supporting Information). Although the alloy exhibits a ΔS_{mix} lower than 1.5R, the thermal stability of the C14-Laves phase predominantly originates from the high temperature and the enthalpic contribution that governs the phase stability through atomic interaction and chemical bonding of the constituents rather than the configurational disorder. Comparable observations have been reported for other C14-Laves phases systems.[24,31,35]

For further confirmation of the formed structure, the geometric and electronic factors were also evaluated, and the corresponding values are shown in **Table S2** (Supporting Information). As demonstrated in previous studies,[16,21,31,36] the criteria to correctly predict the formation of the C14-Laves phase in multicomponent alloys were established as $\delta > 5.0\%$, $1.05 \leq r_A/r_B \leq 1.28$, $5.88 \leq VEC \leq 7.53$, and $\Delta^{\chi}_{Allen} > 7.0\%$. The investigated semiempirical parameters fall reasonably within the appropriate intervals, reinforcing the hypothesis of formation of the C14-Laves phase alloy. It is worth nothing that the parametric approach is more reliable when computing at least three parameters and not only prioritizing one factor over others, to provide a complete thermodynamic picture.[13,25,33] Moreover, it is more practical to assess the likelihood of forming the C14-Laves phase using the confidence maps of these thermodynamic parameters, constrained within the established confidence regions. **Fig. 1** shows the plotted 2D confidence maps of $\Delta H_{mix} - \delta$, $\Omega - \delta$, $VEC - \delta$, $\Delta^{\chi}_{Allen} - \delta$ to directly determine the relationship between these parameters and the targeted phases. The most likely structural domains are indicated by each region's confidence boundaries, which are drawn from previously published data in literature.[13,31,36,37,38,39] The light peach area indicates the formation of solid-solutions (**SS**), the intermetallic domain (**I**) is represented by the pink region, and the coexistence of solid-solution and intermetallics (**SS + I**) is depicted by the light green area. For comparison, the calculated parameters of the predicted C14-Laves $Zr_{28}Ti_7Mn_{30}Fe_{25}Mo_{10}$ alloy are depicted on the diagrams in **Fig. 1**. Although not sufficient to fully explain the formation and stability of the Laves phase, these semiempirical factors still provide an effective prediction of Laves phase formation and provide insights into the alloy's intrinsic properties, substantially reducing the number of experimental trials. For a deeper understanding of these parameters, their

ranges, and other factors not mentioned here, readers are referred to the cited studies.[16,31,36,40]

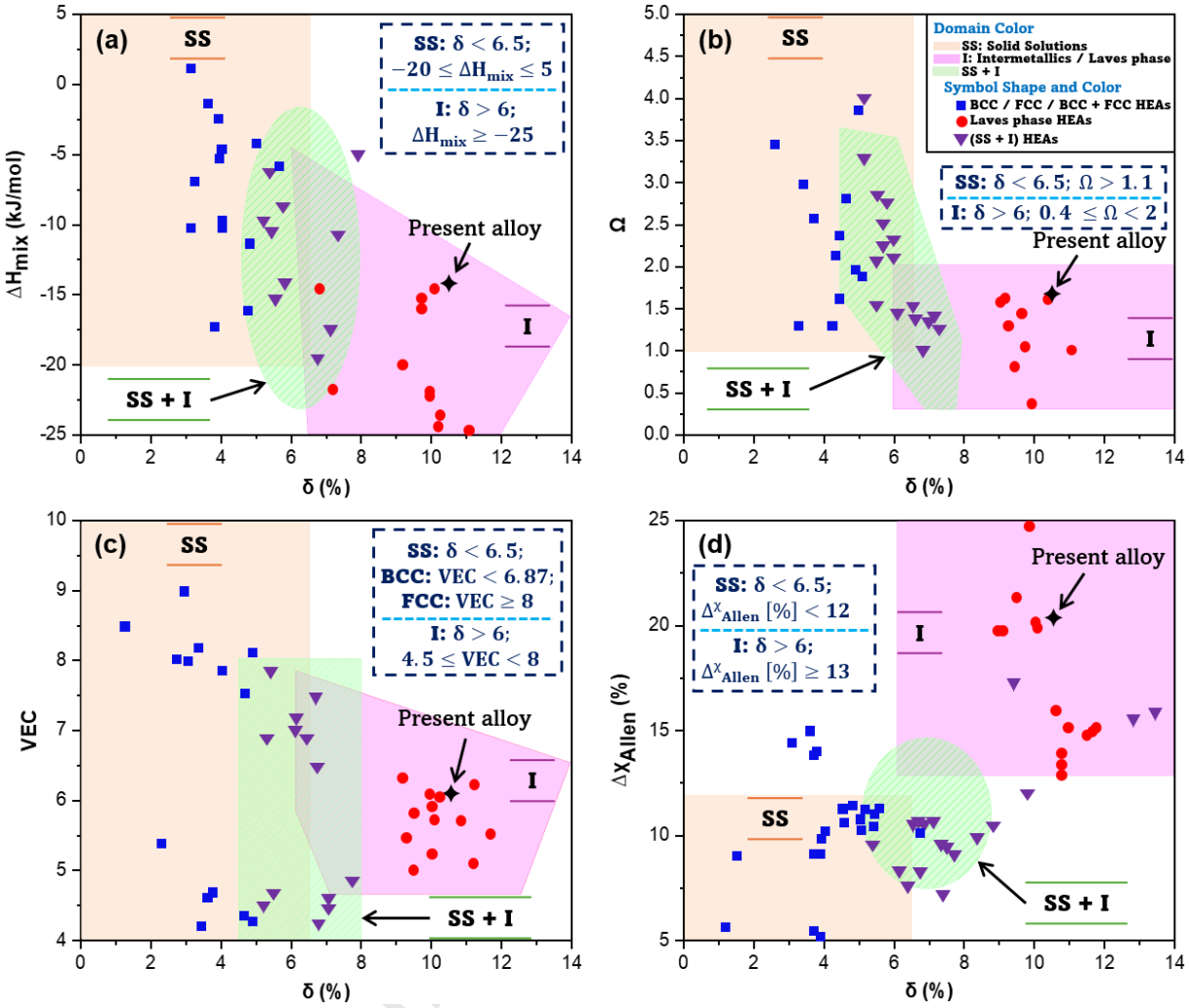


Fig. 1. Empirical 2D maps for phase selection of HEAs based on the relationship between different empirical parameters. (a) Plot of ΔH_{mix} as a function of δ, (b) Plot of Ω as a function of δ, (c) Plot of VEC as a function of δ, and (d) Plot of Δ^{χ}_{Allen} as a function of δ. For comparison, our $Zr_{28}Ti_7Mn_{30}Fe_{25}Mo_{10}$ alloy is represented by a black diamond and the other HEA compositions from literature[13,31,36,37,38,39] are indicated by blue squares for BCC/FCC HEAs, red discs for C14-Laves phase HEAs, and purple triangles for mixed HEAs.

3.1.2. CALPHAD Approach

The stability of the obtained phases during thermodynamic equilibrium was successfully evaluated by the CALPHAD method using the $ThermoCalc^{TM}$ 2024b software and TCHEA7 database for HEAs. The CALPHAD method combines thermodynamic models with validated databases, aiming for finding stable phases

under equilibrium by minimization of the global Gibbs free energy of the system.[41] The solidification was also evaluated using the classical Scheil-Gulliver model and the mobility MOBHEA3 database, assessing the solidification path and segregation tendency during cooling of the title composition. The Scheil model assumes infinitely fast diffusion in the liquid state, while no diffusion occurs in the solid phase, as well as a local equilibrium at the solid-liquid interface, thus reflecting out-of-equilibrium conditions during solidification process, as it is the case in arc melting synthesis. A comparison between the predicted phases in both equilibrium and non-equilibrium simulations and those identified experimentally in the as-cast alloy was made for better understanding of the solidification behavior in the alloy. Since most reported HEAs for hydrogen storage are metastable phases, the Scheil model enables a practical approximation of phase formation during rapid solidification.[15]

Figs. 2a and **2b** show, respectively, the thermodynamic phase diagram as a function of mole percent of Ti for the $(Zr_{1-x}Ti_x)_{35}Mn_{30}Fe_{25}Mo_{10}$ system and the calculated amount of equilibrium phases in mol fraction as a function of temperature for the designed $Zr_{28}Ti_7Mn_{30}Fe_{25}Mo_{10}$ alloy ($x = 0.2$). As can be seen in **Fig. 2a**, the alloy with 7 at.% of Ti solidifies as a primarily C14-Laves phase ($MgZn_2 - P6_3mmc$) under thermodynamic equilibrium. Although the BCC phase begins to grow as the Ti concentration increases, still the entire system should be solidified predominantly as a C14-Laves phase. It is worth mentioning that the phase diagram displays a direct liquid-solid transition without the two phase (L + S) region appearing clearly. This can be explained by the rapid transition from liquid phase to solid phase with negligeable compositional change across a very narrow temperature range. Therefore, the liquid-solid coexistence zone becomes too thin to be visible in the phase diagram. Such behavior resembles the so-called congruent transformation.[42] In **Fig. 2b**, the $Zr_{28}Ti_7Mn_{30}Fe_{25}Mo_{10}$ alloy starts to crystallize at around 1480 °C as a single C14-Laves phase in the equilibrium conditions and remains stable over a wide range of high temperatures ($\approx 1480 - 730\,°C$). Upon cooling below 730 °C, the thermodynamic equilibrium conditions lead to the decomposition of a fraction of the C14-Laves phase into a minor BCC phase. However, this fraction remains low ($< 10\%$), and might be suppressed by the rapid cooling associated with the arc melting process, promoting a single C14-Laves phase under non-equilibrium conditions, as reported previously for other systems.[21,22,43]

Fig. 2c shows the out-of-equilibrium solidification for the $Zr_{28}Ti_7Mn_{30}Fe_{25}Mo_{10}$ alloy. The Scheil calculation indicates that the deviation from thermodynamic equilibrium during solidification leads to the formation of a major C14-Laves phase ($> 95\%$) and a small fraction of BCC_B2 phase as can be deduced from the phase diagram shown in **Fig. 2b**. In addition, this deviation suggests that element segregation may occur upon solidification, where some elements preferentially partition between the solid and liquid phases, resulting in compositional inhomogeneities within the final ingot.[15] Moreover, the large Scheil solidification range ($\approx 266\,°C$) compared to the equilibrium solidification range ($\approx 38.5\,°C$) indicates strong solute partitioning and a high tendency for microsegregation. Nevertheless, since the current Scheil model neglects diffusion in the solid and assumes full diffusion of the solute into the liquid phase, it likely overestimates the extent of segregation.[15,44] In reality, partial back-diffusion and remelting during arc melting are expected to reduce compositional gradients, leading to a more homogeneous single-phase microstructure than predicted by the Scheil model. Overall, the CALPHAD calculations successfully predict and support the formation and stability of a major C14-Laves phase in the title alloy. Microsegregation is also expected to occur during the solidification process. For an in-depth understanding of the CALPHAD approach and Scheil model and their limitations, see the references.[45,46]

3.1.3. Thermodynamic Modeling of PCT diagrams

The PCT model describes the hydrogen storage behavior of alloys through the relationship between hydrogen pressure, hydrogen concentration, and temperature. It allows to estimate the enthalpy and entropy of absorption, and equilibrium pressures, providing valuable insights into thermodynamic properties of such systems during hydrogen sorption under varying operating conditions. This model was first proposed by Zepon et al.[47] to calculate the PCT diagrams of BCC alloys. Then, Ponsoni et al.[16] adapted the same model under relevant conditions to calculate the PCT curves for C14-Laves phase HEAs and tested it for over 400 compositions. As a first approximation, the PCT model for C14-Laves alloys considers hydrogen absorption by the alloy (forming the so-called α-phase), which will be directly linked to occupation of the interstitial sites in the C14-Laves phase structure. It is important to mention that this modeling approach, as a second approximation, is only applicable under para-equilibrium (PE) conditions,[16] where the alloy atoms are nearly immobile, whereas hydrogen atoms remain mobile, see **S3** (Supporting Information).

The PCT model for C14-Laves phase considers, as a third approximation, that only $\mathrm{A_2B_2}$ interstitial sites will form interstitial solid solution as they represent the most energetically favorable interstitial sites for hosting hydrogen atoms in the C14-Laves phase lattice compared to $\mathrm{AB_3}$ and $\mathrm{B_4}$ sites, **Fig. S1** (Supporting Information).[48] Hence, the maximum limit of hydrogen capacity is set to $\mathrm{H/M} = 1$.[16] Additionally, this thermodynamic model assumes that the enthalpy of the C14-Laves phase ($\Delta \mathrm{H_m(c_H)}$) is linearly dependent on hydrogen content. A more detailed explanation of the intermediate equations and parameters along with the calculation of the thermodynamic model and its limitations, can be found in the study of Ponsoni et al.[16] Altogether, considering the above mentioned assumptions, the PCT diagrams can be calculated using Equation (1).

$$ln\left(\frac{P_{H_2}}{P^0}\right) = \frac{2}{RT}\left(h_{C14} - T[-Rln(\frac{c_H}{1-c_H}) - \frac{S^{\circ}_{H_2}}{2}]\right) \quad (1)$$

where P_{H_2}, P^0, R, and T stand for the hydrogen pressure, the referenced pressure (1 atm), the ideal gas constant (8.314 J/mol.K), and the given temperature, respectively. $c_H = \frac{n_H}{n_M}$ is the hydrogen concentration absorbed in the phase, where n_H and n_M are the number of moles of hydrogen and metal atoms in the phase, respectively. h_{C14} is the hydrogen partial molar enthalpy of the C14-Laves phase and it is described as a sum of the contribution of each element in the $\mathrm{A_2B_2}$ tetrahedral sites, see **S3** (Supporting Information). ΔH_i^{∞} is the enthalpy of hydrogen solution at infinite dilution and it represents the approximate contribution of each alloy element's hydrogen partial molar enthalpy, see **Table S1** (Supporting Information). The last term in Equation (1) is the standard entropy of $\mathrm{H_2}$ gas, $S^{\circ}_{H_2}$, see **S3** (Supporting Information).

The idea of describing the h_{C14} by the contribution of the enthalpy of hydrogen solution at infinite dilution for each element, originates from the fact that this thermodynamic model allows the hydrogen absorption only through solid solution. As a result, it ignores the existence of a well-defined plateau pressure where a low concentrated solid-solution (α-phase) and a high hydrogen content hydride (β-phase) are in equilibrium, as reported experimentally in multiple studies.[26,27,49] The obtained value of h_{C14} for the $\mathrm{Zr_{28}Ti_7Mn_{30}Fe_{25}Mo_{10}}$ is $-17.33\ \mathrm{kJ/mol\ H}$. Based on these parameters and on Equation (1), the PCT curves of the $\mathrm{Zr_{28}Ti_7Mn_{30}Fe_{25}Mo_{10}}$ alloy were calculated at 70, 100, and 130 °C as shown in **Fig. 2d**.

The most valuable information extracted from the PCT curves include the maximum hydrogen capacity and equilibrium pressures at the applied temperatures. Achieving high capacities at low pressures can be seen as a competitive advantage.[22] However the alloys should fulfil other criteria such as rapid kinetics, hydrogen desorption at low to mild temperatures, and stability upon cycling. From **Fig. 2d**, the calculated PCT diagram for the $Zr_{28}Ti_7Mn_{30}Fe_{25}Mo_{10}$ alloy highlights slopy curves with no sign for β-phase transition, supporting the fact that the model only considers hydrogen sorption via α-phase. Moreover, the model predicts an equilibrium pressure of approximately 5 MPa (≈ 50 bar) at $H/M = 0.5$ and 70 °C. Under these mild conditions, the alloy might be in a well-balanced thermodynamic state, where hydrogen is neither too weakly nor too strongly bound suggesting its potential thermodynamic reversibility with complete hydrogen desorption upon lowering the hydrogen pressure below the equilibrium pressure. The increase of temperature (100 and 130 °C) shifts the equilibrium pressure to higher values in order to maintain the same absorbed hydrogen capacity, as high temperatures tend to promote hydrogen desorption.[21,33]

In summary, the alloy composition and its initial PCT diagram were designed and calculated, preparing for the experimental investigation its phase composition, microstructure, and hydrogen storage behavior.

Journal Pre-proof

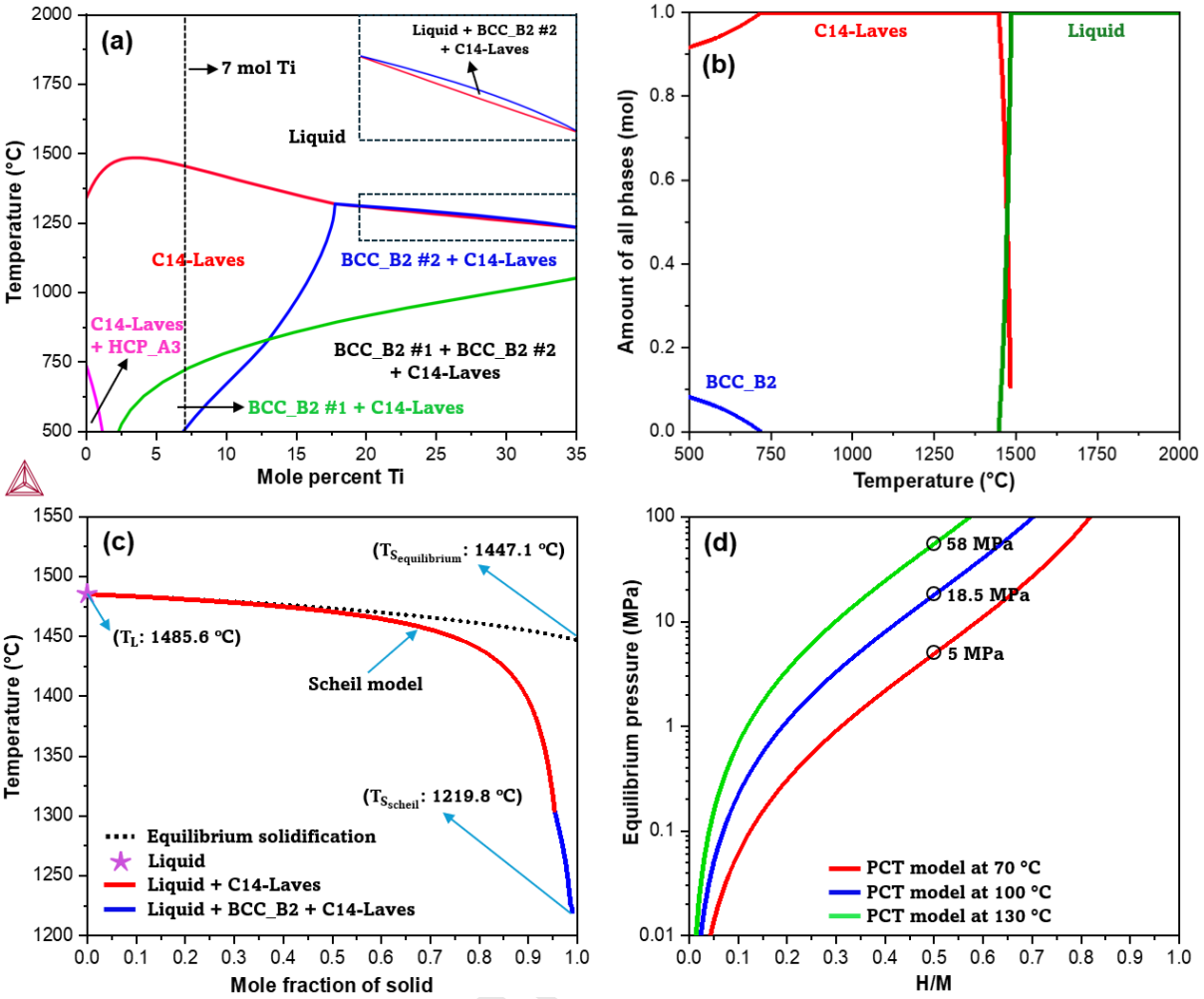
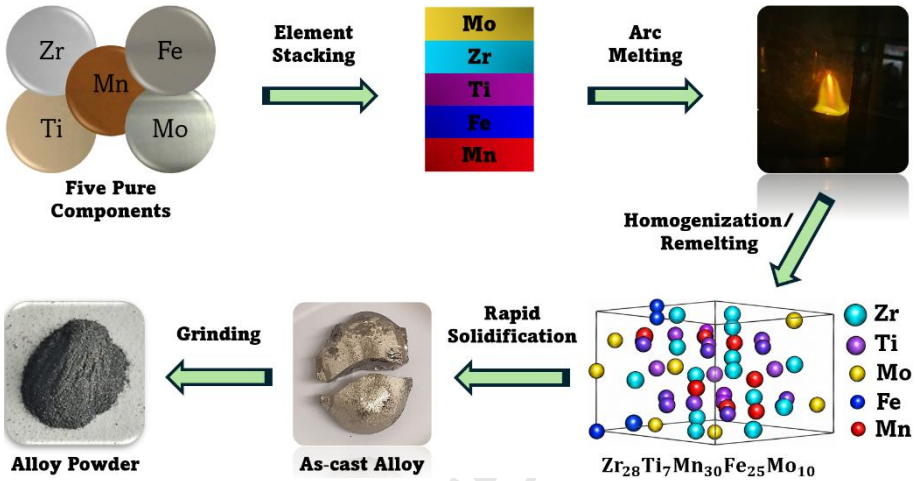


Fig. 2. (a) Thermodynamic phase diagram as a function of mole percent of Ti calculated for the $(Zr_{1-x}Ti_x)_{35}Mn_{30}Fe_{25}Mo_{10}$ system, with 0 ≤ x ≤ 1, (b) Calculated amount of equilibrium phases in mol fraction as a function of temperature for the $Zr_{28}Ti_7Mn_{30}Fe_{25}Mo_{10}$ alloy (x = 0.2). Both diagrams were calculated using CALPHAD and TCHEA7 database, (c) Equilibrium and non-equilibrium (Scheil model) solidification paths predicted by the Gulliver-Scheil model for the $Zr_{28}Ti_7Mn_{30}Fe_{25}Mo_{10}$ alloy, and (d) Calculated PCT diagrams at 70, 100, and 130 °C for the C14-Laves phase $Zr_{28}Ti_7Mn_{30}Fe_{25}Mo_{10}$ alloy. Note that the plateau pressure of the phase transition is not predicted, considering only the filling of the interstitial sites in the α-phase hydride the fact that the hydrogen partial molar enthalpy (h_{C14}) is considered a constant and temperature independent.

3.2. Synthesis, Phase Composition, and Microstructure Analysis

After design, the $Zr_{28}Ti_7Mn_{30}Fe_{25}Mo_{10}$ alloy was synthesized via arc melting, as illustrated in **Scheme 1**. **Table S4** (Supporting Information) shows the composition of the arc melted alloy using ICP-OES analysis. The ICP-OES results are in good

agreement with the nominal composition. With the exception of Mn, which exhibits a deviation of around 2 wt% of its initial weight due to its very low melting point compared to the other elements (see **Table S1** in the supporting information), the rest of elements demonstrate very close weight fractions to their designed values. In addition, no post-synthesis homogenization was applied to the alloy to prevent any oxidation effect or phase decomposition.



Scheme 1. Schematic illustration of the arc melting synthesis protocol for the non-equiatomic $Zr_{28}Ti_7Mn_{30}Fe_{25}Mo_{10}$ alloy.

Following synthesis, the obtained ingot was ground using an abrasive SiC paper to remove any residual oxides and surface contaminants, and subsequently hand crushed into powder using a mortar and pestle. **Fig. 3a** shows the morphology of the $Zr_{28}Ti_7Mn_{30}Fe_{25}Mo_{10}$ alloy particles. It can be seen that the as-crushed powder contains particles with irregular shapes, sharp edges, and form an evenly distribution with particle size ranging between 100 and around 300 μm. This indicates that the alloy is intrinsically brittle.[19,50] **Fig. 3b** shows the XRD pattern with the corresponding Rietveld refinement results for the $Zr_{28}Ti_7Mn_{30}Fe_{25}Mo_{10}$ alloy in the as-cast state. All the diffraction peaks are consistent with the hexagonal C14-Laves phase structure ($MgZn_2-\text{type}$ with space group $P6_3/mmc$), indicating that the alloy mainly crystallizes as a single C14-Laves phase. The sharp diffraction peaks reveal that the as-cast sample is highly crystalline. Although predicted by the thermodynamic phase diagram, there are no visible reflections from secondary BCC phase in the XRD profile, demonstrating the reliability of the arc melting synthesis method in achieving single C14-Laves phase alloys. Similar findings were reported in previous works by other authors.[21,22,51]

The calculated composition and constitution of each element in the C14 unit cell via the CALPHAD method are shown in **Table S3** (Supporting Information) and were used as a basis in the Rietveld refinement. **Table S5** (Supporting Information) gives the structural parameters of the C14-Laves phase, as determined by the Rietveld refinement: $a = 0.506\,\mathrm{nm}$ and $c = 0.829\,\mathrm{nm}$. In addition, the XRD peaks reveal small broadening, likely attributed to local chemical heterogeneities resulting from segregation during solidification. The same observation was reported by Ponsoni et al.[21] These observations are in good agreement with the Scheil model simulation (**Fig. 2c**), confirming the predicted segregation and its effect on the broadening of the XRD reflections. Overall, the XRD analysis demonstrates that the $Zr_{28}Ti_7Mn_{30}Fe_{25}Mo_{10}$ alloy crystallizes as a single C14-Laves phase multicomponent alloy.

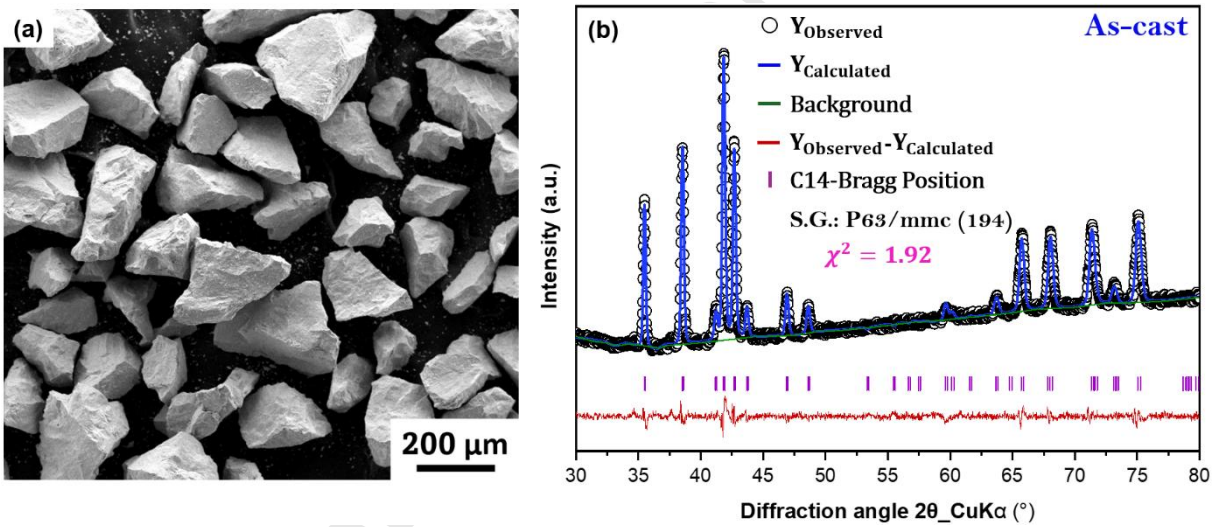


Fig. 3. (a) SEM-SE image of the as-cast $Zr_{28}Ti_7Mn_{30}Fe_{25}Mo_{10}$ alloy and (b) X-ray diffraction pattern and the Rietveld refinement of the as-cast $Zr_{28}Ti_7Mn_{30}Fe_{25}Mo_{10}$ alloy (Experimental and calculated XRD patterns are shown by a black circle and a blue line, respectively, their difference is highlighted by the dark red line, and the background of the data is shown by a green line).

To examine the microstructural features of the as-cast $Zr_{28}Ti_7Mn_{30}Fe_{25}Mo_{10}$ alloy, a bulk sample was mounted in a conductive resin, ground using successive abrasive SiC papers and finely polished with diamond suspensions, followed by chemical etching using HF-based solution. **Fig. 4a** shows the SEM back-scattered micrograph of the studied alloy. It can be observed that the $Zr_{28}Ti_7Mn_{30}Fe_{25}Mo_{10}$ exhibits a dendritic microstructure, typical of most C14-Laves phase alloys produced by the arc

melting method.[20,21,26] **Fig. 4b** highlights a higher magnification BSE image of a localized zone within the microstructure. It is clear that there is a difference in color contrast between the dendritic and interdendritic regions, signifying a local chemical inhomogeneity. The bright gray “A” area corresponds to the matrix phase which is the dendritic zone and the dark gray “B” area is the interdendritic zone which was preferentially attacked as seen in **Fig. 4b**. Quantitative elemental EDX of the different regions are shown in **Table S6** (Supporting Information).The overall chemical composition is close to the nominal one with the exception of Mn that shows lower at% which is in agreement with the previous ICP-OES results. Besides, the measured chemical composition in the interdendritic zone “B” is richer in Ti and poorer in Zr and Mo compared to the dendritic region “A”. In contrast, the dendritic zone is richer in Zr and Mo and poorer in Ti. By looking into the corresponding EDX maps shown in **Fig. 5a**, it can be seen that Zr, Ti, and Mo are not homogenously distributed across the microstructure. Meanwhile, Mn and Fe are found to be uniformly distributed between the “A” and “B” regions. Such behavior has been also reported in several studies for C14-Laves phase alloys that show a gradient in chemical compositions which leads to a distribution of lattice constants and hence peak broadening.[22,52] Furthermore, the alloy microstructure contains some Zr-oxide inclusions, probably formed during melting or during sample preparation, and the presence of small Zr-rich clusters, **Fig. 4b**. Although the alloy exhibited a single C14-Laves phase, the observed Ti segregation remains consistent with the XRD patterns and can be explained by the strong solute portioning during solidification that promotes high tendency of microsegregation and thereby chemical gradient within the microstructure as already predicted by the Scheil model in **Fig. 2c**.

The alloy microstructure was further examined by TEM analysis. **Fig. 5b** exhibits a bright-field TEM image obtained from the as-cast $Zr_{28}Ti_7Mn_{30}Fe_{25}Mo_{10}$ sample. The particle shown in this image reveals a nanocrystalline microstructure as confirmed in the corresponding selected area electron diffraction (SEAD) pattern of **Fig. 5c**, which is indexed as C14-Laves phase with hexagonal structure and space group $P6_3/mmc$, supporting well the XRD results (**Fig. 3b**). Similar observations were reported by Fontana et al.[53] The presence of nanostructures in the alloy sample is further consistent with the broadening of the XRD peaks of the C14-Laves phase in **Fig. 3b**. The high-resolution HR-TEM image acquired from the red rectangle in **Fig. 5b**, thereby confirms the formation of the C14-Laves as the major phase as depicted in

Fig. 5d. The measured d-spacing of $0.253\ \mathrm{nm}$ corresponds to the (110) plane of the C14-Laves phase. To further support the final microstructure of the investigated alloy, additional TEM analyses were performed. **Fig. S3** (Supporting Information) shows BF-TEM and HAADF-STEM images, together with the corresponding SAED pattern, indicating the presence of one phase in the $Zr_{28}Ti_7Mn_{30}Fe_{25}Mo_{10}$ alloy. **Fig. S4** (Supporting Information) presents the STEM-EDX mapping, which reveal a homogeneous distribution of the constituent elements. These complementary results further support the findings presented above, indicating that the alloy exhibits a predominantly single-phase microstructure.

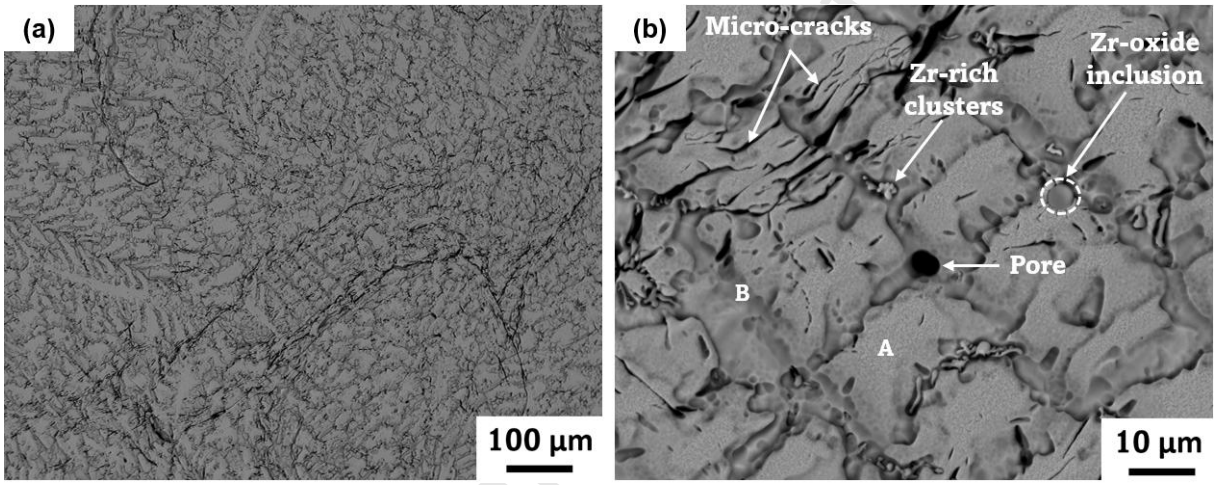


Fig. 4. (a-b) SEM-BSE micrographs at different magnifications of the as-cast $Zr_{28}Ti_7Mn_{30}Fe_{25}Mo_{10}$ alloy after chemical etching.

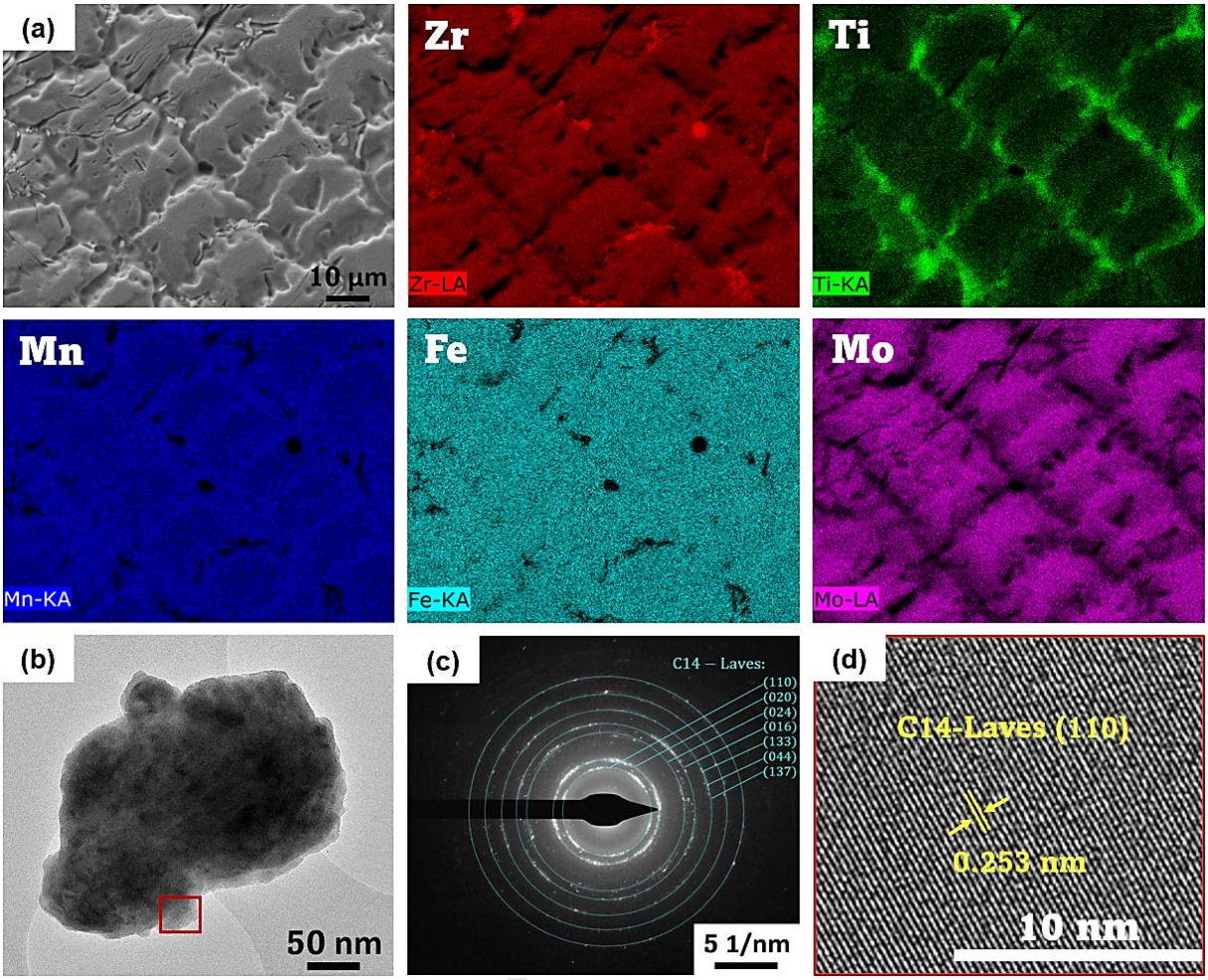


Fig. 5. Microstructural characterization of the as-cast $Zr_{28}Ti_7Mn_{30}Fe_{25}Mo_{10}$ alloy: (a) SEM-SE micrograph and corresponding elemental EDX maps. TEM images: (b) Bright-field TEM image, (c) Selected area electron diffraction pattern image, and (d) HR-TEM image.

3.3. Hydrogen Storage Properties

3.3.1. PCT Measurements and Thermodynamic Properties

To better understand the hydrogen storage behavior of the $Zr_{28}Ti_7Mn_{30}Fe_{25}Mo_{10}$ alloy, PCT measurements were first performed using a Sieverts-type apparatus to evaluate the hydrogen absorption and desorption properties at 70, 100, and 130 °C up to a maximum hydrogen pressure of 10 MPa, as illustrated in **Fig. 6a** (see Experimental Section for more details). Prior to PCT tests, the alloy sample was activated by heating under a dynamic vacuum at 200 °C for 2 hours, followed by one hydrogen absorption/desorption cycle at 130 °C up to 10 MPa. After activation, absorption/desorption PCT measurements were carried out sequentially at 130, 100, and 70 °C, with intermediate degassing after each cycle for few minutes under

dynamic vacuum at 200 °C to ensure complete desorption of residual hydrogen. Notably, the same sample was employed for all hydrogen measurements at the three investigated temperatures. **Fig. 6a** shows the three hydrogenation/dehydrogenation PCT isotherms of the $Zr_{28}Ti_7Mn_{30}Fe_{25}Mo_{10}$ alloy at 130, 100, and 70 °C. Under a maximum hydrogen pressure of 10 MPa, the alloy reaches hydrogenation saturation for all temperatures, which is commonly around 1 H/M for C14-Laves type structures. Additionally, with increasing temperature, the maximum hydrogen capacity decreases from 1.56 wt% ($H/M = 1.08$) at 70 °C to 1.48 wt% ($H/M = 1.03$) at 100 °C, and 1.43 wt% ($H/M = 0.99$) at 130 °C. Meanwhile, the equilibrium pressure measured at $H/M = 0.5$ shows a strong temperature dependence, rising from 0.07 MPa at 70 °C to 0.19 MPa at 100 °C, and 0.46 MPa at 130 °C. These phenomena are quite common and are thermodynamically driven effects, where the reduction of the hydrogen capacity at elevated temperatures is directly linked to the increase in equilibrium pressure.[15,20,21,22]

On the other hand, no full desorption was observed at both 70 and 100 °C temperatures, implying partial retention of the absorbed hydrogen within the alloy. In addition, incomplete desorption is particularly much more pronounced at 70 °C. As shown in **Fig. 6a**, at this temperature, the equilibrium pressure is approximately 0.07 MPa, below atmospheric pressure, suggesting that the dehydrogenation process would likely become increasingly difficult as the equilibrium pressure decreases and the driving force for desorption diminishes. Similar behavior has been reported in previous studies.[19,23] Accordingly, the relatively high equilibrium plateau pressures of the alloy under the applied desorption conditions may favor hydrogen release,[21,22,49] see **Table 1**. Furthermore, the PCT curves display relatively low hysteresis between hydrogenation and dehydrogenation paths, especially at lower temperatures. In general, hysteresis in PCT isotherms is an intrinsic property of hydrides which mainly originates from the elastic strain of crystal lattice during hydrogen uptake and release processes.[23] Upon hydrogen absorption, the lattice stress increases which slows the hydrogen diffusion and hinders the desorption process. As a result, a higher pressure difference is needed to drive the dehydrogenation reaction.[23] These observations further support the incomplete desorption curves at low temperatures. At 130 °C, the alloy absorbs and desorbs hydrogen almost reversibly with negligeable hysteresis. This behavior is attributed to the enhanced lattice expansion at elevated

temperatures, which reduces the lattice stress and provides more space for hydrogen storage, and thereby mitigates the hysteresis effect.[54]

It is worth to point out that the PCT diagrams clearly reveal the presence of a well-defined equilibrium plateau pressure-like region, extending from 0.20 to ~ 0.90 wt%, for all temperatures. This behavior indicates that hydrogen absorption in the investigated alloy probably occurs via both interstitial solid-solution (α-phase) and hydride (β-phase) nucleation. Such mechanism has been reported in several earlier studies.[15,26,49] Conversely, many C14-Laves phase HEAs have shown a very sloping plateau pressure, indicating hydrogen absorption solely via interstitial sites which induces a gradual expansion of the crystal lattice without the presence of an equilibrium plateau between the metal and hydride phases.[19,20,23] From a thermodynamic point of view, the enthalpy and entropy for hydrogen absorption and desorption of the $Zr_{28}Ti_7Mn_{30}Fe_{25}Mo_{10}$ alloy were determined via the well-known van't Hoff plot calculated for equilibrium pressures at $H/M = 0.5$. **Fig. 6b** shows the van't Hoff curves and the estimated thermodynamic data are given in **Table S7** (Supporting Information). The values of ΔH_{Abs}, ΔS_{Abs}, ΔH_{Des}, and ΔS_{Des} are -36.1 kJ/mol H_2, -101.8 J/(K mol) H_2, $+34.3$ kJ/mol H_2, and $+96.6$ J/(K mol) H_2, respectively. These calculations demonstrate that both the enthalpy and entropy do not change significantly between hydrogen absorption and desorption. A similar thermodynamic trend has been observed in the TiVFeZr multicomponent alloy.[20] Furthermore, the obtained values are closely comparable to those reported for the benchmark $LiNi_5$[55] alloy and fall within the moderate thermodynamic ranges commonly observed for C14-Laves phase HEAs (typically, $-40 \ll \Delta H \ll -30$ kJ/mol H_2 and $-85 \ll \Delta S \ll -110$ J/(K mol) H_2),[56] suggesting moderate hydride stability and favorable reversibility under moderate temperature and pressure conditions.

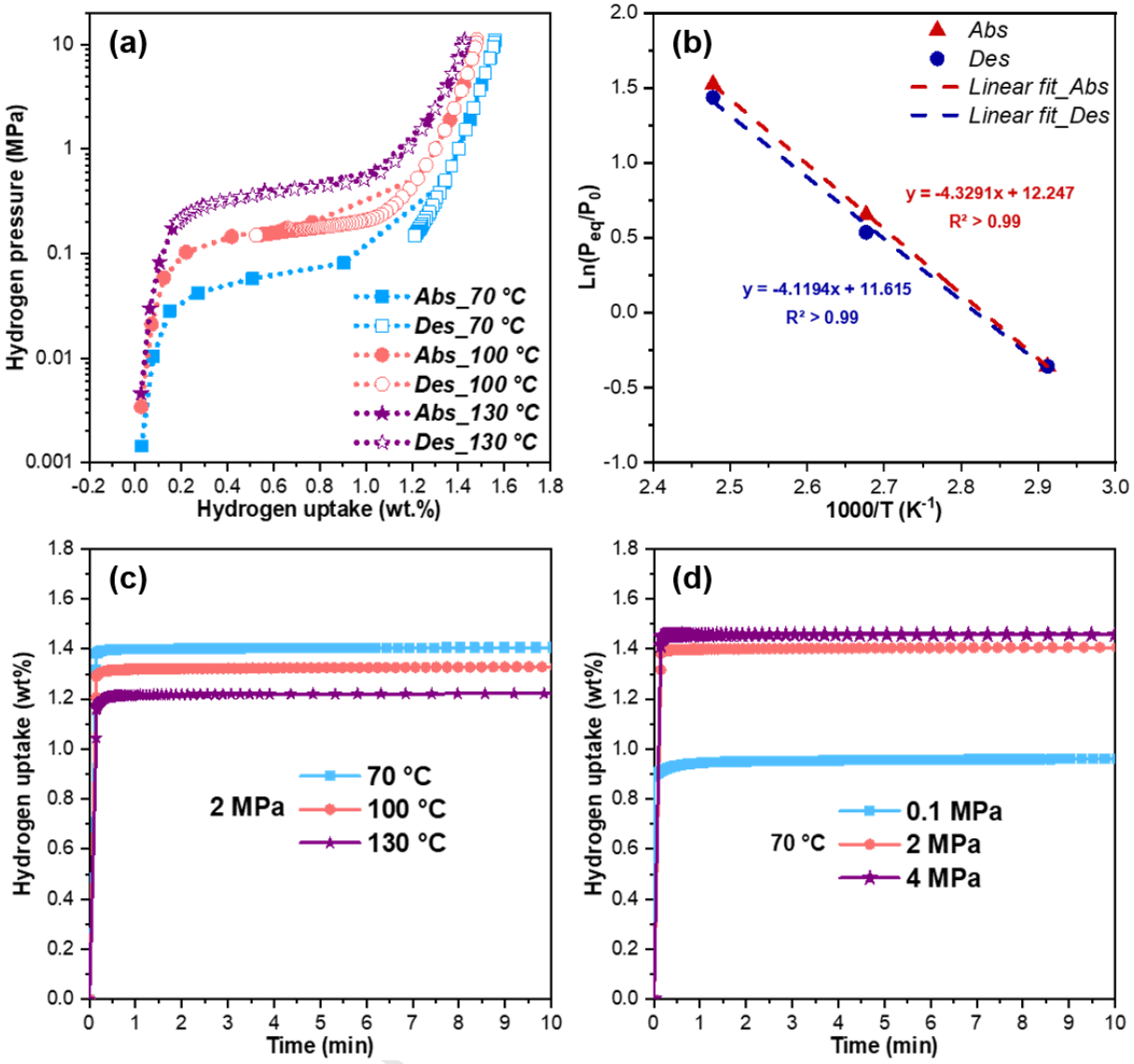


Fig. 6. (a) Absorption/desorption PCT isotherms for the $Zr_{28}Ti_7Mn_{30}Fe_{25}Mo_{10}$ alloy at 70, 100, and 130 °C. (b) Van't Hoff plot for the $Zr_{28}Ti_7Mn_{30}Fe_{25}Mo_{10}$ alloy using the equilibrium pressure at 0.5 H/M during absorption and desorption reactions. Hydrogen absorption kinetics curves of the $Zr_{28}Ti_7Mn_{30}Fe_{25}Mo_{10}$ alloy in the first cycle: (c) at different temperatures (70, 100, and 130 °C) under 2 MPa hydrogen pressure and (d) at 70 °C under different hydrogen pressures (0.1, 2, and 4 MPa).

3.3.2. Hydrogen Absorption Kinetics and Capacity

Fig. 6c presents the hydrogen absorption kinetics curves of the $Zr_{28}Ti_7Mn_{30}Fe_{25}Mo_{10}$ alloy carried out at 70, 100, and 130 °C under a hydrogen pressure of 2 MPa after activation. The alloy absorbs hydrogen extremely fast upon exposure to H_2 molecules, exhibiting no noticeable incubation time for all temperatures. Such behavior can be primarily attributed to the prior activation procedure, which involved

thermal treatment followed by one absorption/desorption PCT cycle at 130 °C. This activation process likely facilitated subsequent hydrogen uptake by improving the accessibility of hydrogen absorption sites and promoting H-alloy atoms interactions, as reported for other alloys showing similar fast absorption kinetics following activation with almost no incubation period.[20,21,24] These observations highlight the importance of the activation procedure in achieving the fast hydrogen chemisorption kinetics observed in the present alloy, reaching 99% of its total capacity in only few seconds. Furthermore, the very rapid hydrogen absorption kinetics across all investigated temperatures may also be associated with the intrinsic structural features of the C14-Laves phase, including large (δ = 10.55%) lattice distortion, microsegregation, and grain boundaries within the polycrystalline structure suggested by the continuous rings in the SAED pattern as observed in the SAED patterns (**Fig. 5b**). Altogether, these microstructural features may serve simultaneously as fast diffusion pathways and preferential hydride nucleation sites in addition to tetrahedral interstitial sites, and further contribute to the enhanced hydrogen absorption kinetics.[25,57,58,59]

In addition, the alloy was able to achieve an absorption capacity of 1.40 wt% ($\mathrm{H/M} = 0.97$) at 70 °C under 2 MPa of hydrogen pressure, which is comparable to values reported for other C14-Laves HEAs, such as $\mathrm{Ti_{21}Zr_{21}Fe_{41}Ni_{17}}$,[24] TiVZrNbFe,[60] and $(\mathrm{Ti_{0.33}Zr_{0.33}Nb_{0.33}})_1(\mathrm{Mn_{0.5}Cr_{0.5}})_2$[21] that were able to absorb 1.40 wt% at RT under 3.5 MPa of $\mathrm{H_2}$, 1.36 wt% at 200 °C under 1 MPa of $\mathrm{H_2}$, and 1.35 wt% at 25 °C under 3.6 MPa of $\mathrm{H_2}$, respectively. From a compositional standpoint, the $\mathrm{Zr_{28}Ti_7Mn_{30}Fe_{25}Mo_{10}}$ alloy exhibits higher content of Zr than Ti. Since Zr has a more negative hydrogen enthalpy of formation compared to Ti ($\Delta H_f(ZrH_2) = -163$ kJ/mol $\mathrm{H_2}$[61] and $\Delta H_f(TiH_2) = -122.3$ kJ/mol $\mathrm{H_2}$[62]), this compositional feature further enhances the hydrogen absorption kinetics and capacity, especially at low temperature-pressure conditions.[27] However, this strong bonding between Zr and H atoms might contribute to incomplete release of a fraction of hydrogen in the alloy.[28]

To evaluate the effect of hydrogen pressure on the hydrogen absorption capacity of the alloy, kinetic measurements were conducted at 70 °C under 0.1, 2, and 4 MPa of hydrogen pressure, as shown in **Fig. 6d**. It is evident that the maximum hydrogen storage uptake increases with the increase of the hydrogen pressure, reaching up to 0.96 wt% ($\mathrm{H/M} = 0.66$), 1.40 wt% ($\mathrm{H/M} = 0.97$), and 1.46 wt% ($\mathrm{H/M} = 1.01$), at 0.1,

2, and 4 MPa, respectively. Remarkably, the alloy can absorb more than 0.90 wt% under only 0.1 MPa, highlighting the important role of prior activation and the significant thermodynamic affinity of hydrogen for the Zr-rich C14-Laves phase lattice. This behavior suggests the potential of the present alloy for low-pressure hydrogen storage applications.

3.3.3. Hydrogen Desorption Behavior

The hydrogen desorption behavior of the hydrogenated $Zr_{28}Ti_7Mn_{30}Fe_{25}Mo_{10}$ alloy is investigated by conducting DSC and TGA analyses under an inert gas (Ar) atmosphere with a constant heating rate of 5 °C/min from RT to 600 °C. The alloy sample was fully hydrogenated at 70 °C under 10 MPa of hydrogen pressure. **Fig. 7a** shows the DSC curve during desorption process. The analysis reveals that the DSC signal shows a broad endothermic feature associated with a small shoulder at around 216 °C, indicating a moderate temperature at which the formed C14-Laves hydrides start to decompose.[20] Additionally, the gradual heat-flow decrease might be related to the continuous release of hydrogen from different tetrahedral interstitial sites with different distribution of binding energies. The TGA result is represented in **Fig. 7b** and highlights a pronounced mass loss around 200 °C, corresponding to hydrogen release from the hydride interstitial sites, which is in good consistency with the DSC results and pointing towards moderate thermodynamic stability of hydrogen in the alloy. The total mass loss during heating was approximately 0.46 wt% ($H/M = 0.32$), much lower than the absorption capacity measured at 10 MPa in **Fig. 6a** (1.56 wt% ($H/M = 1.08$)). Since the DSC and TGA analyses were carried out under atmospheric pressure (0.10 MPa) and considering the fact that the equilibrium hydrogen pressure is much lower than 0.10 MPa, the alloy would naturally tend to desorb hydrogen very fast at such pressure. After reaching the maximum weight loss at around 240 °C, the sample started to gain weight which might be due to possible oxidation reaction of the hydrogenated sample probably related to the Ar purity.[9]

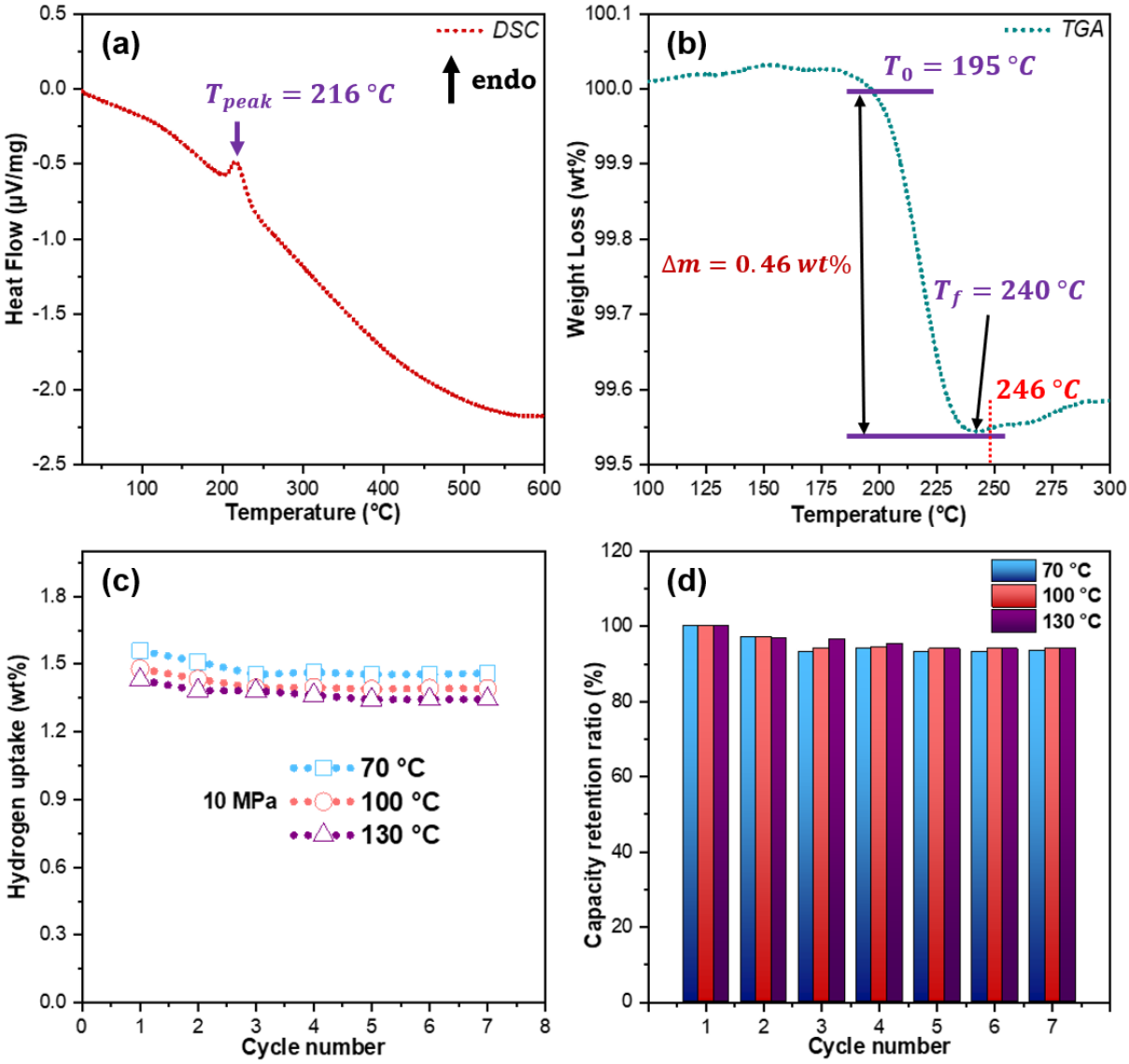


Fig. 7. The dehydrogenation behavior of $Zr_{28}Ti_7Mn_{30}Fe_{25}Mo_{10}$ hydrides at a constant heating rate of 5 °C/min under Ar atmosphere: (a) DSC measurement from RT to 600 °C and (b) TGA pattern from 100 to 300 °C. Absorption/desorption cycling performance of the $Zr_{28}Ti_7Mn_{30}Fe_{25}Mo_{10}$ alloy: (c) PCT curves after the first and the 7th cycle at 70, 100 , and 130 °C and (d) Change in hydrogen storage capacity as function of the number of cycles.

3.3.4. Hydrogenation Cycling Properties

To study the $Zr_{28}Ti_7Mn_{30}Fe_{25}Mo_{10}$ alloy's hydrogen absorption/desorption reversibility and the temperature-dependent cycling behavior, 7 PCT cycles of absorption/desorption at 70, 100, and 130 °C were evaluated. The hydrogen absorption was conducted at all temperatures under a maximum hydrogen pressure of 10 MPa and the hydrogen desorption process was carried out at 200 °C under a dynamic vacuum for few minutes. **Figs. 7c** and **7d** depict the maximum hydrogen

uptake and absorption capacity retention for the different cycles. At 70 °C, the hydrogen absorption capacity decreases slightly from 1.56 wt% in the 1st cycle to 1.51 wt% in the 2nd cycle, and 1.45 wt% in the 3rd cycle, then maintained fixed until the 7th cycle as shown in **Fig. 7c**. The same behavior is observed for the cycling at 100 °C. However, at 130 °C, the hydrogen capacity drops from 1.43 wt% (1st cycle) to 1.38 wt% (2nd cycle), remains stable in the 3rd cycle, then gradually declines to 1.34 wt% by the 5th cycle and stabilizes thereafter, indicating the effect on temperature on the cycling performance. From **Fig. 7d**, it can be seen that, for all temperatures, the alloy showed a capacity retention after 7 cycles of more than 94%, which highlights the good reversibility of the alloy at all temperatures. Nevertheless, the small drop in the hydrogen storage capacity retention ratio might be attributed to the applied moderate temperature during the dehydrogenation process (200 °C).[20] Chen et al.[19] reported that their alloy $\mathrm{TiZrFeMnCrV}$ can reversibly store up to 97% of its initial capacity after 50 cycles when conducting the desorption process at 350 °C under dynamic vacuum for 30 min. Similar behavior was reported for other C14-Laves alloys.[20,63] In addition, upon cycling many crystal defects are created which also contribute to a fraction of the hydrogen to be trapped in the alloy.[33] Besides, we believe that applying a higher desorption temperature (i.e.; above 400 °C) can lead to zero loss of absorption capacity. Furthermore, Pan et al.[54] reported in their study that besides the above mentioned effects, the hydrogen purity (99.999% in the present study) can also affect the capacity of the alloy, especially if it contains small amounts of impurities such as nitrogen which might react and lead to a reduction of the hydrogen overall capacity. It should be noted that hydrogen storage reversibility at low temperatures is also related to the VEC of HEAs. Edalati et al.[26] reported that a VEC of 6.40 promotes the reversibility at RT of the alloy during cycling without the need for heating. In the present study, the developed alloy has a VEC value of 6.10; its lower value may contribute to the incomplete hydrogen reversibility. A comparison of the hydrogen storage performance of the investigated alloy with other C14-Laves HEAs is given in **Table 1**. Moreover, it is worth mentioning that the seven hydrogenation/dehydrogenation cycles in the present work were intended to provide a preliminary assessment of the alloy's cycling performance at different temperatures and its structural stability, rather than a comprehensive evaluation of its long-term durability. Overall, the non-equiatomic $\mathrm{Zr_{28}Ti_7Mn_{30}Fe_{25}Mo_{10}}$ alloy has demonstrated a hydrogen storage capacity of 1.56 wt% at 70 °C with minor decrease in its cycling

performance, indicating its good cycling stability after 7 PCT cycles under the applied moderate temperatures compared to other HEAs that exhibits such stability only at 30°C.[20,21,53,57] These results highlight the potential of the $Zr_{28}Ti_7Mn_{30}Fe_{25}Mo_{10}$ alloy as a promising candidate for low pressure hydrogen storage applications.

Table 1. Comparative hydrogen storage properties of some other Zr/Ti-based HEAs. All these alloys are majorly single C14-Laves phase and are synthesized via the arc melting method.

HEA composition	VEC	Temperature (°C)	$P_{eq_{abs}}$ (MPa) at 0.50 H/M	H/M_{max} (wt%)	Reference
$(Ti_{0.33}Zr_{0.33}Nb_{0.33})_1(Mn_{0.5}Cr_{0.5})_2$	6.40	70	2.62	1.35	[21]
$(Ti_{0.5}Zr_{0.5})_1(Fe_{0.33}Mn_{0.33}Cr_{0.33})_2$	6.00	60	1.30	1.66	[22]
$Ti_{0.84}Zr_{0.16}Mn_{0.9}Cr_{0.7}Fe_{0.1}$	6.55	25	0.92	1.83	[54]
$Ti_{0.29}Zr_{0.05}Al_{0.05}Cr_{0.26}Mn_{0.35}$	6.40	35	0.86	1.76	[15]
$Ti_{20}Zr_{20}Mn_{20}Fe_{20}Co_{20}$	6.40	30	0.20	1.60	[64]
$TiZrCrFeMnNi$	6.40	32	0.90	1.70	[26]
$Zr_{28}Ti_7Mn_{30}Fe_{25}Mo_{10}$	6.10	70	0.07	1.56	Present study

In order to check the structural stability of the $Zr_{28}Ti_7Mn_{30}Fe_{25}Mo_{10}$ alloy after 7 hydrogenation cycles at 70 °C, the samples at the hydrogenated and dehydrogenated states were examined by XRD analysis, as shown in **Fig. 8 and Fig. S6 (**Supporting Information), respectively. Similar to the metallic $Zr_{28}Ti_7Mn_{30}Fe_{25}Mo_{10}$ alloy, the hydride maintained its original phase composition after cycling, indicating good structural stability of the investigated alloy, as seen in **Fig. 8a**. However, the XRD pattern shows wider peaks with decreased intensity, which is likely due to increased lattice stress or grain refinement.[21,54] Interestingly, the Rietveld refinement reveals that the hydrogenated alloy exhibits two distinct C14-Laves phases ($P6_3/mmc$), hereafter named C14#1(α-phase) and C14#2 (β-phase), corresponding to the hydride formed at the first stage of hydrogenation through solid-solution with low concentration of hydrogen and the hydride phase formed during equilibrium with high H concentration (main hydride), respectively, **Fig. 8c**. The lattice parameters and phase fractions are listed in **Table S5** (Supporting information file). The C14#1(α-phase) structure accounts for 72 wt% with slightly higher lattice parameters ($a =$

$0.508\,\mathrm{nm}$, $c = 0.832\,\mathrm{nm}$) compared to the as-cast state, resulting in the $AB_2H_{0.24}$ hydride ($H/M \approx 0.08$), as shown in **Fig. 8b**, which corresponds to the slight peak shift towards lower angles. Meanwhile, the C14#2 (β-phase) contributes with 28 wt% in the C14-Laves phase, but with larger parameters ($a = 0.535\,\mathrm{nm}$, $c = 0.874\,\mathrm{nm}$), corresponding to a volume expansion of 20% of the formed $AB_2H_{2.83}$ hydride (**Fig. 8b)**. This volume expansion corresponds to a hydrogen uptake of 0.94 H/M ($\approx 1.36\,\mathrm{wt\%}$), by taking into account $2.9\,\text{Å}^3/H$ as a volume increment.[21] Furthermore, the reason behind having higher fraction of the $AB_2H_{0.24}$ hydride, with a small change in the lattice volume, is the fact that the alloy rapidly releases hydrogen upon exposure to atmospheric pressure, even though the XRD analysis was done immediately after hydrogenation. Such observations were reported in Andrade et al.[24] and Aranda et al.[20] studies.

Fig. S6 (Supporting Information) compares the XRD patterns of the $Zr_{28}Ti_7Mn_{30}Fe_{25}Mo_{10}$ alloy in the as-cast, hydrogenated, and dehydrogenated states, together with the corresponding lattice parameters of the C14-Laves phase obtained by Rietveld refinement, see **Table S5 (**Supporting Information). After seven hydrogenation cycles, the fully dehydrogenated sample retained its single C14-Laves phase, with no detectable changes in the lattice parameters. These results demonstrate further the alloy's good structural stability and support its reversibility under the investigated conditions. Furthermore, the small amount of residual hydrogen, corresponding to a capacity retention ratio of 94% in **Fig. 7d**, was released during evacuation prior to XRD characterization, allowing the lattice parameters to return to their initial values.

Journal Pre-proof

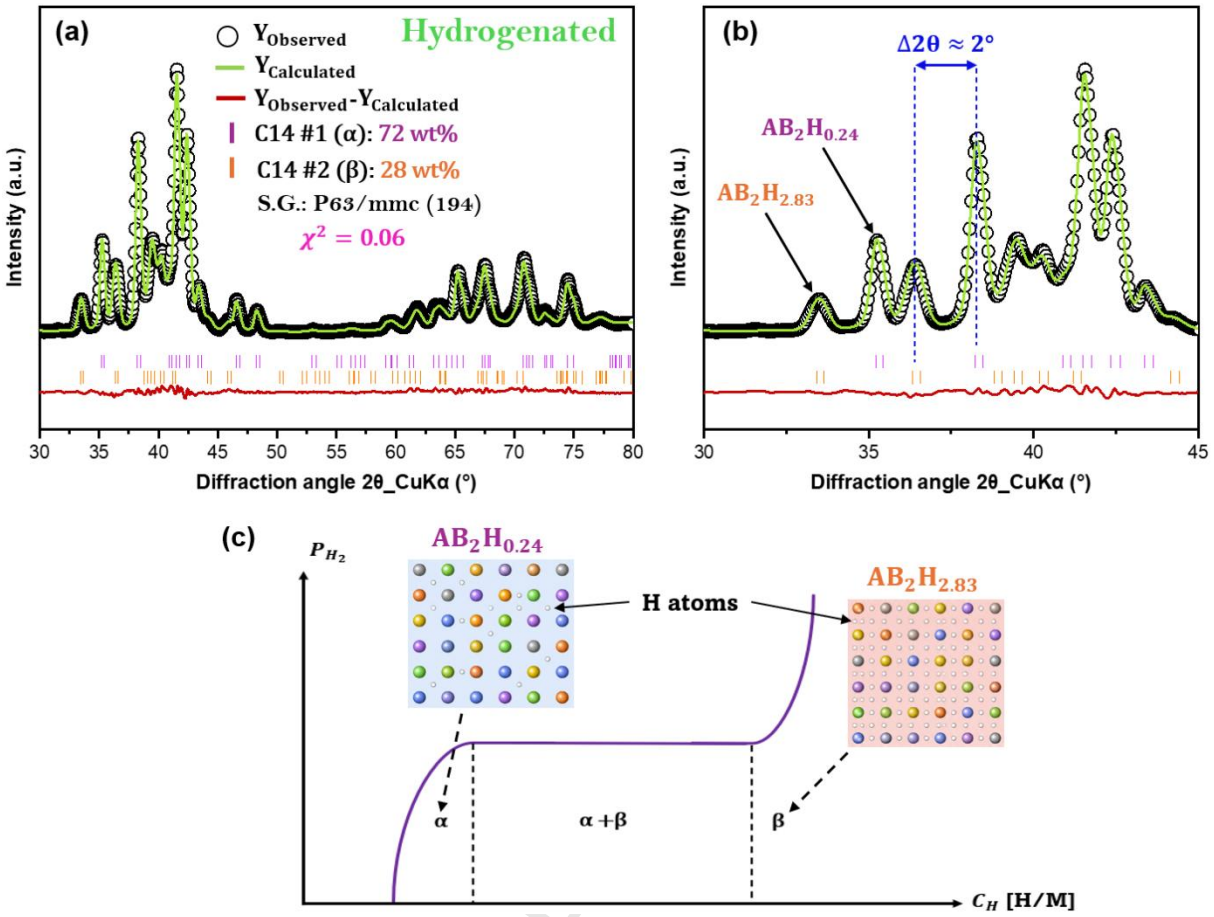


Fig. 8. (a-b) XRD pattern of the $Zr_{28}Ti_7Mn_{30}Fe_{25}Mo_{10}$ alloy in the hydrogenated state after 7 absorption/desorption cycles at 70 °C and (c) Typical PCT curve showing the three stages of hydrogenation with schematic illustrations of the two C14-Laves hydrides (C14#1(α-phase) and C14#2 (β-phase)) extracted from the Rietveld refinement.

Fig. 9 shows the microstructural investigations of the $Zr_{28}Ti_7Mn_{30}Fe_{25}Mo_{10}$ alloy particles before and after hydrogenation cycles. Before charged into the Sievert's cell, the as-cast ingot was crushed easily into powder as shown in **Fig. 9a**, due to its intrinsic brittleness. The particles show an average particle size of around 166 µm (**Fig. 9c**) with irregular shapes, sharp edges, and no visible cracks on the surface as can be seen in **Fig. 9b**. **Fig. 9d** shows the alloy powder after seven PCT cycles of hydrogen absorption and desorption. The particle size obviously decreased dramatically to approximately 16 µm (**Fig. 9f**), and cracks and fragmentations are more pronounced on the surface of the particles as shown in **Fig. 9e**. This phenomenon is the main consequence of the volume expansion that generates severe lattice strain during hydrogen uptake and release leading to a repeated

expansion/contraction within the host alloy. Upon cycling the lattice stress induces cracks that nucleate and propagate leading to embrittlement. Such behavior is well known for the C14-Laves HEAs.[21,22,23,54] It is worth mentioning that the presence of chemical segregation (**Fig. 5**) in the microstructure facilitates crack initiation due to local stress and hydrogen-induced lattice expansion between two different regions. Nevertheless, cracks can have a positive impact on the activation properties as they shorten the diffusion distance, increase the contact area between the fine particles and H molecules, and thereby fasten the absorption kinetics.[23,59] As mentioned earlier, hydrogenation cycling induces grain refinement and increases crystal defects, which promotes rapid hydrogen kinetics and activation, however, it also leads to a slight reduction in the overall capacity due to irreversible hydrogen trapping at these defects as shown in **Fig. 7c**.

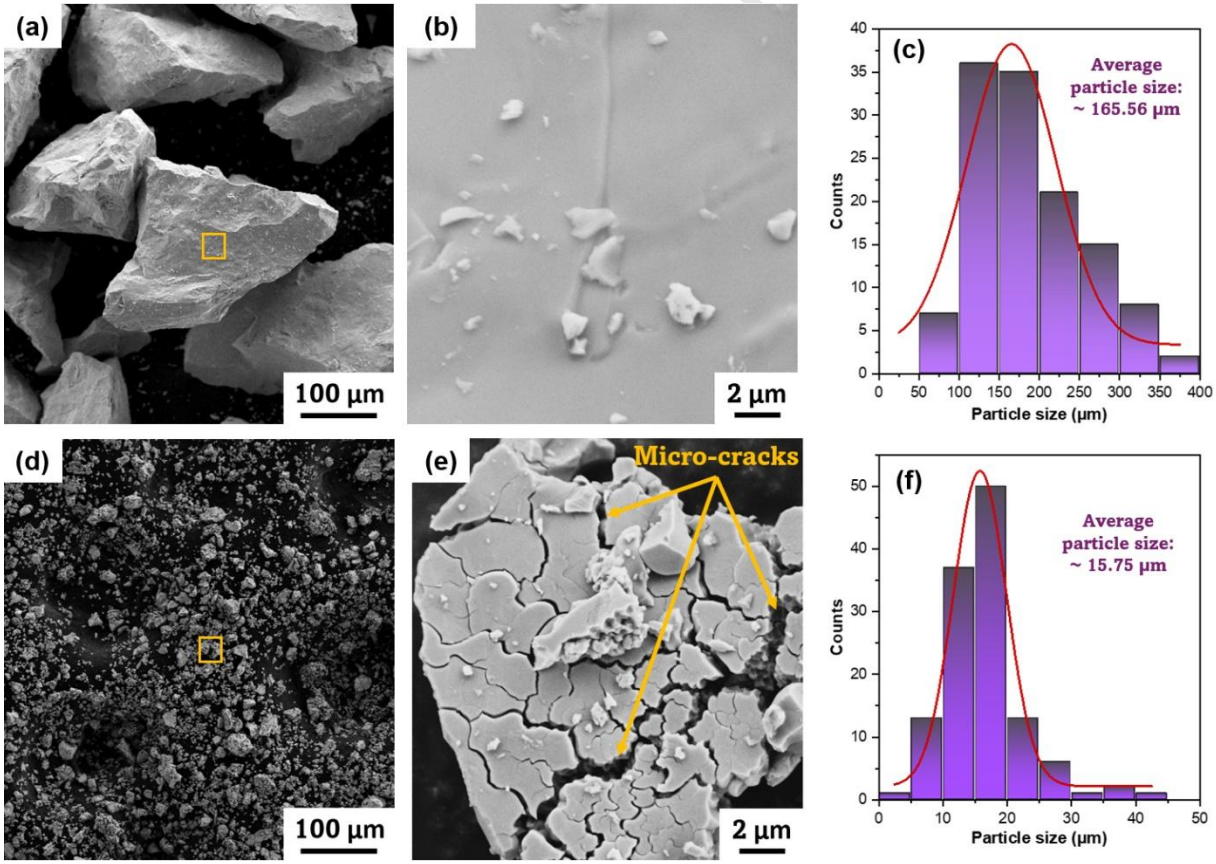


Fig. 9. SEM-SE images of the $Zr_{28}Ti_7Mn_{30}Fe_{25}Mo_{10}$ alloy particles: (a-b) prior to hydrogenation and (d-e) after 7 hydrogenation/dehydrogenation cycles. Average particle size of the $Zr_{28}Ti_7Mn_{30}Fe_{25}Mo_{10}$ alloy: (c) before hydrogenation and (f) after the 7th absorption/desorption cycle.

3.3.5. Comparison of experimental and modeled PCT curves

The initially calculated PCT curves at 70, 100, and 130 °C shown in **Fig. 2d** are compared with experimentally measured hydrogen absorption PCT diagrams. **Fig. 10a** shows the results for the $Zr_{28}Ti_7Mn_{30}Fe_{25}Mo_{10}$ multicomponent alloy. Clear differences can be observed between the curves with respect to their shape, maximum hydrogen capacity, and the equilibrium pressure at $H/M = 0.5$. Such discrepancies are reasonable and can be attributed to the set of simplifying assumptions underlying the first thermodynamic model (Section 3.1.3.). The absence of a distinct plateau pressure in the calculated PCT curves arises primarily from the hydrogen partial molar enthalpy (h_{C14}), which was assumed to be constant and temperature independent as described in the work of Ponsoni et al.[16] Therefore, the initial thermodynamic model cannot adequately reproduce the behavior of the PCT curve seen experimentally. Thus, there is a need to refine the initial description to account for the observed hydrogenation behavior. Accordingly, the model was further refined using the experimental data, resulting in a more improved reproduction of the experimental PCT isotherms. In fact, in their work, Marques et al.[15] found that h_{C14} has a linear behavior and it depends on temperature. Which was the case in the current study, it was found that the hydrogen partial molar enthalpy (h_{C14}) is not a constant as can be seen in **Fig. S7a** (Supporting Information). Instead, it could be better approximated to a linear behavior as described by the following Equation (2):[15]

$$h_{C14} = h_{0.5} + h_1(c_H - 0.5) \quad (2)$$

where $h_{0.5}$ is the value of h_{C14} at a hydrogen uptake ($c_H(H/M)$ of 0.5 and h_1 is the factor that will account for the change in the shape of the PCT curves that the initial model from Ponsoni et al.[16] could not reproduced. Such improvement in the model is with great importance to validate the calculation for our present work. Being said, the main part now is to determine the values of the parameters $h_{0.5}$ and h_1. For this raison, we used the method of least squares (Equation (11) in **S3,** Supporting Information) in first stage to estimate the values of h_{C14} from Equation (1). Unlike the work of Marques et al.[15], where they extracted the values of h_{C14} only from experimental PCT curves at 35 °C assuming that the h_{C14} in independent of temperature. Here, however, we have estimated the values of this later at each temperature (70, 100, 130 °C) as we observed that the factors $h_{0.5}$ and h_1 are not constant with temperature, see **Fig. S7b** (Supporting Information). After obtaining the

first estimations of these parameters, the method of direct least squares (DLS) is used again in the case of equilibrium pressure (P_{H_2}) to estimate the optimized values of the parameters $h_{0.5}$ and h_1 that minimize the difference between the values of h_{C14} obtained from the fitting of the experimental PCT curves at each temperature and the calculated values from Equation (2). For more details about the calculations and equations, readers are referred to the work of Marques et al.[15] It should be mentioned that in the later study, the authors used the method of least squares to calculate $h_{0.5}$ and h_1 for each elements (A-type and B-type) as their study include a series of stoichiometries, whereas in this work we have only one composition.

Based on the obtained parameters and Equations (1 and 2), the PCT diagrams were calculated at 70, 100, 130°C and were compared with the experimental ones as shown in **Fig. 10b**. For all temperatures, the PCT models reproduce the experimental ones more accurately thanks to the proposed linear behavior of h_{C14} as a function of the hydrogen content and the dependency of this latter on temperature, resulting in achieving, with good precision, similar shape, appearance of the plateau-like region, and the equilibrium plateau pressures. This simplified approach has a crucial role to investigate the hydrogen storage applicability of C14-Laves alloys through the estimation of the range of equilibrium pressures at different moderate temperatures. Nevertheless, one of the limitations of this approach is the fact that h_{C14} does not preserve its linear behavior at low/or high hydrogen contents (**Fig. S7a**, Supporting Information). Although, in the current study, the deviation of the model from the experience was not present that much, suggesting that the refined model's assumptions can be valid for other C14-laves stoichiometries within the Zr-Ti-Mn-Fe-Mo system. Overall, the enhanced approach provides a useful framework for investigating hydrogen storage behavior of related C14-Laves alloys with promising potential for hydrogen storage applications.

Journal Pre-proof

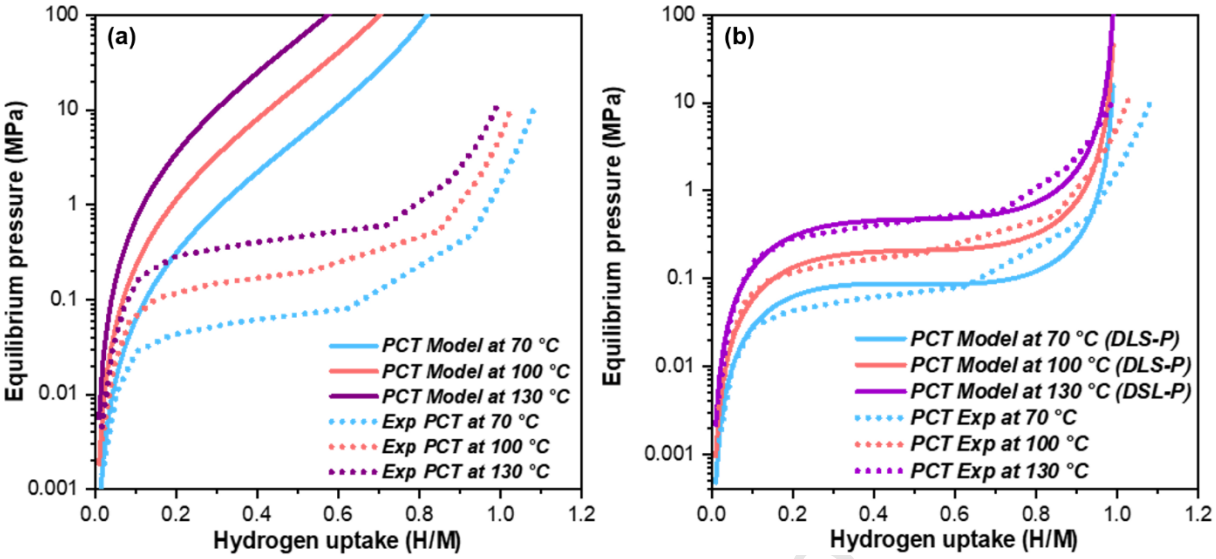


Fig. 10. Comparison between experimental and calculated PCT diagrams of the $Zr_{28}Ti_7Mn_{30}Fe_{25}Mo_{10}$ alloy at 70, 100, and 130 °C. (a) based on the initial predictive model and (b) based on the refined model using the least-squares method. In the calculated PCT curves (**Fig. 10b**), the partial molar enthalpy (h_{C14}) is considered temperature dependent which shows the good agreement of the model with the experiments at all temperatures.

4. Concluding Remarks

In this work, a combined design approach integrating computational and semiempirical parameters was successfully applied to develop the non-equiatomic $Zr_{28}Ti_7Mn_{30}Fe_{25}Mo_{10}$ multicomponent alloy. The alloy was synthesized by arc melting and experimentally confirmed to crystallize predominantly as a single C14-Laves phase, in good agreement with the design predictions. Microstructural analyses revealed a dendritic and nanostructured morphology with local chemical segregation, which contributes to lattice distortion and defect formation, both playing a key role in the hydrogen storage behavior.

Volumetric hydrogen sorption measurements demonstrated that the alloy exhibits attractive storage performance under moderate temperature–pressure conditions. A maximum hydrogen capacity of 1.56 wt% ($H/M = 1.08$) was achieved at 70 °C under 10 MPa, while equilibrium pressures increased from 0.07 MPa at 70 °C to 0.46 MPa at 130 °C (at $H/M = 0.5$). The presence of a plateau-like region in the PCT isotherms indicates a mixed hydrogenation mechanism involving both interstitial solid solution and hydride ($\alpha - \beta$) formation

The alloy exhibits extremely fast hydrogenation kinetics, reaching nearly full capacity within seconds and showing no noticeable incubation time. This remarkable behavior is attributed to the prior activation procedure, which involved thermal treatment followed by one absorption/desorption PCT cycle at 130 °C, in addition to the microstructural features, including the severe lattice distortion ($\delta \approx 10.51\%$), nano-structuring, and microsegregation-induced defect network, which enhance hydrogen diffusion and provide favorable nucleation sites. Collectively, a significant hydrogen uptake ($> 0.9\ wt\%$) at near-ambient pressure was achieved, reflecting the important role of prior activation and the significant thermodynamic affinity of hydrogen for the Zr-rich C14-Laves phase lattice.

Thermodynamic analysis using van't Hoff relations revealed moderate hydride stability, with absorption and desorption enthalpies of approximately $-36\ \mathrm{kJ/mol\ H_2}$ and $+34\ \mathrm{kJ/mol\ H_2}$, respectively. These values are consistent with reversible hydrogen storage at moderate temperatures, although complete desorption is limited at low temperatures due to the low equilibrium pressure. Complementary DSC/TGA analyses confirmed that hydrogen release occurs at around $200 - 220\ ℃$, indicating that moderate heating is required to ensure full reversibility.

The alloy also demonstrates good cycling and structural stabilities, retaining more than 94% of its initial capacity after seven absorption/desorption cycles. Despite hydrogen-induced lattice expansion ($\sim 20\%$) and particle pulverization, the C14-Laves phase is preserved in both hydrogenated and dehydrogenated states, confirming its structural robustness. The observed particle size reduction and crack formation during cycling further enhance hydrogen kinetics, although a small fraction of hydrogen may be irreversibly trapped at defects.

Overall, the $\mathrm{Zr_{28}Ti_7Mn_{30}Fe_{25}Mo_{10}}$ alloy offers a favorable combination of low equilibrium pressure, fast kinetics, and good cycling performance, making it a promising candidate for hydrogen storage applications under moderate operating conditions. The discrepancies between initial modeled and experimental PCT curves have been solved with good precision from the refined model that accurately, captures the shape and plateau-like region consistent with a mixed absorption mechanism (α–β transition). Future work should focus on compositional tuning, adjustment of electronic parameters (e.g., VEC), and microstructural engineering,

including the introduction of secondary phases such as BCC phase to enhance the capacity and to shift the plateau pressure and enhance the reversibility.

Acknowledgements

The authors are grateful to the LACAMI platform at UCLouvain and its staff for providing technical assistance and access to processing and characterization facilities. The authors would like to thank the OCP Foundation for the financial support. H. I. is mandated by the Belgian National Fund for Scientific Research (FSR-FNRS). Y. F. acknowledges FNRS (CC J.0078.24) and SPW-Economie Emploi Recherche for Win4Excellence project “TiNTHyN” under contract No. 2310142. G.E. is FRIA grantee of the FNRS (Belgium).

Conflict of Interest

There are no conflicts of interest to declare.

Data Availability Statement

All data that support the findings of this study are available upon reasonable request from the corresponding author.

References

(1) Dalei, N. N.; Gupta, A. Adoption of Renewable Energy to Phase down Fossil Fuel Energy Consumption and Mitigate Territorial Emissions: Evidence from BRICS Group Countries Using Panel FGLS and Panel GEE Models. *Discov. Sustain.* **2024**, *5* (1), 52. https://doi.org/10.1007/s43621-024-00237-y

(2) Hossain Bhuiyan, M. M.; Siddique, Z. Hydrogen as an Alternative Fuel: A Comprehensive Review of Challenges and Opportunities in Production, Storage, and Transportation. *Int. J. Hydrog. Energy* **2025**, *102*, 1026–1044. https://doi.org/10.1016/j.ijhydene.2025.01.033

(3) Asim, A. M.; Awad, A. S. A.; Attia, M. A. Integrated Optimization of Energy Storage and Green Hydrogen Systems for Resilient and Sustainable Future Power Grids. *Sci. Rep.* **2025**, *15* (1), 25656. https://doi.org/10.1038/s41598-025-09408-x

(4) Kovač, A.; Paranos, M.; Marciuš, D. Hydrogen in Energy Transition: A Review. *Int. J. Hydrog. Energy* **2021**, *46* (16), 10016–10035. https://doi.org/10.1016/j.ijhydene.2020.11.256

(5) Gunathilake, C.; Soliman, I.; Panthi, D.; Tandler, P.; Fatani, O.; Ghulamullah, N. A.; Marasinghe, D.; Farhath, M.; Madhujith, T.; Conrad, K.; Du, Y.; Jaroniec, M. A Comprehensive Review on Hydrogen Production, Storage, and Applications. *Chem. Soc. Rev.* **2024**, *53* (22), 10900–10969. https://doi.org/10.1039/D3CS00731F

(6) Hirscher, M.; Yartys, V. A.; Baricco, M.; Bellosta von Colbe, J.; Blanchard, D.; Bowman, R. C.; Broom, D. P.; Buckley, C. E.; Chang, F.; Chen, P.; Cho, Y. W.; Crivello, J.-C.; Cuevas, F.; David, W. I. F.; de Jongh, P. E.; Denys, R. V.; Dornheim, M.; Felderhoff, M.; Filinchuk, Y.; Froudakis, G. E.; Grant, D. M.; Gray, E. MacA.; Hauback, B. C.; He, T.; Humphries, T. D.; Jensen, T. R.; Kim, S.; Kojima, Y.; Latroche, M.; Li, H.-W.; Lototskyy, M. V.; Makepeace, J. W.; Møller, K. T.; Naheed, L.; Ngene, P.; Noréus, D.; Nygård, M.

M.; Orimo, S.; Paskevicius, M.; Pasquini, L.; Ravnsbæk, D. B.; Veronica Sofianos, M.; Udovic, T. J.; Vegge, T.; Walker, G. S.; Webb, C. J.; Weidenthaler, C.; Zlotea, C. Materials for Hydrogen-Based Energy Storage – Past, Recent Progress and Future Outlook. *J. Alloys Compd.* **2020**, *827*, 153548. https://doi.org/10.1016/j.jallcom.2019.153548

(7) Webb, C. J.; Humphries, T. D.; Teprovich, J. A.; Polanski, M.; Heere, M.; Li, H.-W.; Felderhoff, M.; Filinchuk, Y.; Dornheim, M.; Paskevicius, M.; Buckley, C. E.; Jensen, T. R. Diverse Hydrogen Chemistry with Perspectives for Energy Storage. *Chem. Commun.* **2026**, *62* (15), 4477–4495. https://doi.org/10.1039/D5CC05834A

(8) Broom, D. P. Hydrogen-Based Materials for Energy Storage and Conversion.

(9) Shen, H.; Hu, J.; Li, P.; Huang, G.; Zhang, J.; Zhang, J.; Mao, Y.; Xiao, H.; Zhou, X.; Zu, X.; Long, X.; Peng, S. Compositional Dependence of Hydrogenation Performance of Ti-Zr-Hf-Mo-Nb High-Entropy Alloys for Hydrogen/Tritium Storage. *J. Mater. Sci. Technol.* **2020**, *55*, 116–125. https://doi.org/10.1016/j.jmst.2019.08.060

(10) Marques, F.; Balcerzak, M.; Winkelmann, F.; Zepon, G.; Felderhoff, M. Review and Outlook on High-Entropy Alloys for Hydrogen Storage. *Energy Environ. Sci.* **2021**, *14* (10), 5191–5227. https://doi.org/10.1039/D1EE01543E

(11) Stein, F.; Leineweber, A. Laves Phases: A Review of Their Functional and Structural Applications and an Improved Fundamental Understanding of Stability and Properties. *J. Mater. Sci.* **2021**, *56* (9), 5321–5427. https://doi.org/10.1007/s10853-020-05509-2

(12) Yartys, V. A.; Lototskyy, M. V. Laves Type Intermetallic Compounds as Hydrogen Storage Materials: A Review. *J. Alloys Compd.* **2022**, *916*, 165219. https://doi.org/10.1016/j.jallcom.2022.165219

(13) Aalami, B. E.; Idrissi, H.; Trabadelo, V. C14-Laves Phase High Entropy Alloys for Hydrogen Storage: A Review. *Mater. Horiz.* **2026**, *13* (8), 3721–3760. https://doi.org/10.1039/D5MH01719J

(14) Bellon Monsalve, D.; Kefi, C.; Klopcic, N.; Huot, J. Review of Hydrogen Storage Using AB, AB2, HEA, and Solid Solution Metal Hydrides. *Int. J. Hydrog. Energy* **2026**, *229*, 154686. https://doi.org/10.1016/j.ijhydene.2026.154686

(15) Marques, F.; Zepon, G.; Petersen, H.; Felderhoff, M. Design, Synthesis, and Characterization of Al-Containing Multicomponent Alloys for Hydrogen Storage and Compression. *Adv. Energy Mater.* **2024**, *14* (42), 2401491. https://doi.org/10.1002/aenm.202401491

(16) Ponsoni, J. B.; Aranda, V.; Nascimento, T. D. S.; Strozi, R. B.; Botta, W. J.; Zepon, G. Design of Multicomponent Alloys with C14 Laves Phase Structure for Hydrogen Storage Assisted by Computational Thermodynamic. *Acta Mater.* **2022**, *240*, 118317. https://doi.org/10.1016/j.actamat.2022.118317

(17) Lenis, J. A.; Arias Velandia, J.; Aguirre Ocampo, R.; Zuleta Gil, A. A.; Bello, S.; Correa, E.; Arrieta, C.; Bolívar, F. J.; Echeverría Echeverría, F. Challenges and Potential Future Trends on High Entropy Alloy for Solid Hydrogen Storage: Systematic Review. *J. Power Sources* **2025**, *656*, 238011. https://doi.org/10.1016/j.jpowsour.2025.238011

(18) Kunce, I.; Polanski, M.; Bystrzycki, J. Structure and Hydrogen Storage Properties of a High Entropy ZrTiVCrFeNi Alloy Synthesized Using Laser Engineered Net Shaping (LENS). *Int. J. Hydrog. Energy* **2013**, *38* (27), 12180–12189. https://doi.org/10.1016/j.ijhydene.2013.05.071

(19) Chen, J.; Li, Z.; Huang, H.; Lv, Y.; Liu, B.; Li, Y.; Wu, Y.; Yuan, J.; Wang, Y. Superior Cycle Life of TiZrFeMnCrV High Entropy Alloy for Hydrogen Storage. *Scr. Mater.* **2022**, *212*, 114548. https://doi.org/10.1016/j.scriptamat.2022.114548

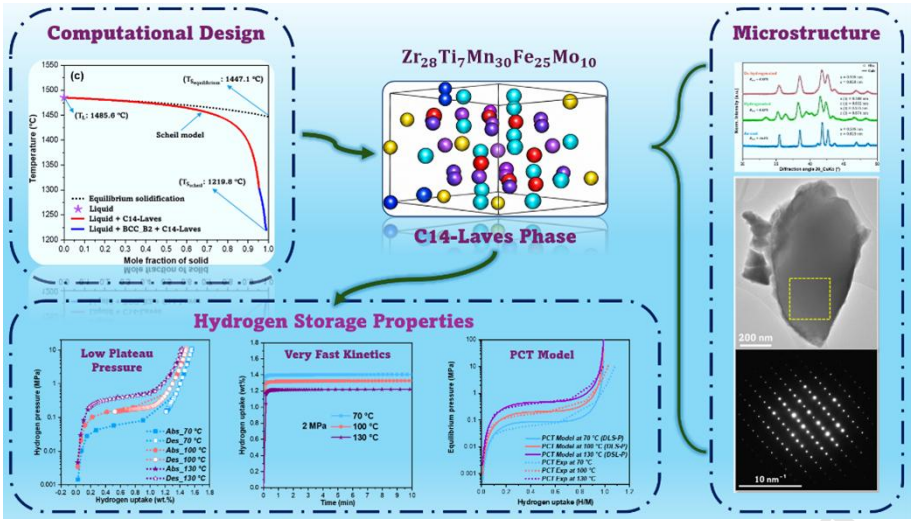
(20) Aranda, V.; Leiva, D. R.; Huot, J.; Botta, W. J.; Zepon, G. Hydrogen Storage Properties of the TiVFeZr Multicomponent Alloy with C14-Type Laves Phase Structure. *Intermetallics* **2023**, *162*, 108020. https://doi.org/10.1016/j.intermet.2023.108020

(21) Ponsoni, J. B.; Aranda, V.; Botta, W. J.; Zepon, G. Reversible Hydrogen Storage at Moderate Pressure–Temperature Conditions of C14 Laves Phase Alloys of the (Ti0.5–xZr0.5–xNb2x)1(Mn0.5Cr0.5)2 System. *ACS Appl. Energy Mater.* **2025**, *8* (12), 8351–8364. https://doi.org/10.1021/acsaem.5c00876

(22) Ponsoni, J. B.; Balcerzak, M.; Botta, W. J.; Felderhoff, M.; Zepon, G. A Comprehensive Investigation of the $(Ti_{0.5}Zr_{0.5})_1(Fe_{0.33}Mn_{0.33}Cr_{0.33})_2$ Multicomponent Alloy for Room-Temperature Hydrogen Storage Designed by Computational Thermodynamic Tools. *J. Mater. Chem. A* **2023**, *11* (26), 14108–14118. https://doi.org/10.1039/D3TA02197A
(23) Zhao, H.; Yao, P.; Zhao, Y.; Zeng, Z.; Xia, C.; Yang, T. Microstructure and Hydrogen Storage Properties of Zr-Based AB2-Type High Entropy Alloys. *J. Alloys Compd.* **2023**, *960*, 170665. https://doi.org/10.1016/j.jallcom.2023.170665
(24) Andrade, G.; Edalati, P.; Dangwal, S.; Edalati, K.; Floriano, R. Microstructural Characterization and Hydrogen Storage Properties at Room Temperature of Ti21Zr21Fe41Ni17 Medium Entropy Alloy. *ACS Appl. Energy Mater.* **2025**, *8* (4), 2033–2042. https://doi.org/10.1021/acsaem.4c02468
(25) Ma, X.; Ding, X.; Chen, R.; Gao, X.; Su, Y.; Cui, H. Enhanced Hydrogen Storage Properties of $ZrTiVAl_{1-x}Fe_x$ High-Entropy Alloys by Modifying the Fe Content. *RSC Adv.* **2022**, *12* (18), 11272–11281. https://doi.org/10.1039/D2RA01064J
(26) Edalati, P.; Floriano, R.; Mohammadi, A.; Li, Y.; Zepon, G.; Li, H.-W.; Edalati, K. Reversible Room Temperature Hydrogen Storage in High-Entropy Alloy TiZrCrMnFeNi. *Scr. Mater.* **2020**, *178*, 387–390. https://doi.org/10.1016/j.scriptamat.2019.12.009
(27) Andrade, G.; Silva, B. H.; Zepon, G.; Floriano, R. Hydrogen Storage Properties of Zr-Based Multicomponent Alloys with C14-Laves Phase Structure Derived from the Zr–Cr–Mn–Fe–Ni System. *Int. J. Hydrog. Energy* **2024**, *51*, 246–254. https://doi.org/10.1016/j.ijhydene.2023.11.111
(28) Ma, X.; Ding, X.; Chen, R.; Zhang, J.; Song, Q.; Cui, H. Microstructural Features and Improved Reversible Hydrogen Storage Properties of ZrTiVFe High-Entropy Alloy via Cu Alloying. *Int. J. Hydrog. Energy* **2023**, *48* (7), 2718–2730. https://doi.org/10.1016/j.ijhydene.2022.10.130
(29) Luo, L.; Chen, L.; Li, L.; Liu, S.; Li, Y.; Li, C.; Li, L.; Cui, J.; Li, Y. High-Entropy Alloys for Solid Hydrogen Storage: A Review. *Int. J. Hydrog. Energy* **2024**, *50*, 406–430. https://doi.org/10.1016/j.ijhydene.2023.07.146
(30) Shahi, R. R.; Gupta, A. K.; Kumari, P. Perspectives of High Entropy Alloys as Hydrogen Storage Materials. *Int. J. Hydrog. Energy* **2023**, *48* (56), 21412–21428. https://doi.org/10.1016/j.ijhydene.2022.02.113
(31) Mishra, S. S.; Yadav, T. P.; Srivastava, O. N.; Mukhopadhyay, N. K.; Biswas, K. Formation and Stability of C14 Type Laves Phase in Multi Component High-Entropy Alloys. *J. Alloys Compd.* **2020**, *832*, 153764. https://doi.org/10.1016/j.jallcom.2020.153764
(32) Guo, S.; Liu, C. T. Phase Stability in High Entropy Alloys: Formation of Solid-Solution Phase or Amorphous Phase. *Prog. Nat. Sci. Mater. Int.* **2011**, *21* (6), 433–446. https://doi.org/10.1016/S1002-0071(12)60080-X
(33) Komeili, M.; Arabi, H.; Pourarian, F. Structural Investigation and Hydrogenation Properties of TiZrXMnFeNi (X = Cr, Mo, and W) High Entropy Alloys. *J. Alloys Compd.* **2023**, *967*, 171672. https://doi.org/10.1016/j.jallcom.2023.171672
(34) Takeuchi, A.; Inoue, A. Mixing Enthalpy of Liquid Phase Calculated by Miedema's Scheme and Approximated with Sub-Regular Solution Model for Assessing Forming Ability of Amorphous and Glassy Alloys. *Intermetallics* **2010**, *18* (9), 1779–1789. https://doi.org/10.1016/j.intermet.2010.06.003
(35) Zareipour, F.; Shahmir, H.; Huang, Y.; Patel, A. K.; Dematteis, E. M.; Baricco, M. Hydrogen Storage in TiVCr(Fe,Co)(Zr,Ta) Multi-Phase High-Entropy Alloys. *Int. J. Hydrog. Energy* **2024**, *94*, 639–649. https://doi.org/10.1016/j.ijhydene.2024.11.109
(36) Yurchenko, N.; Stepanov, N.; Salishchev, G. Laves-Phase Formation Criterion for High-Entropy Alloys. *Mater. Sci. Technol.* **2017**, *33* (1), 17–22. https://doi.org/10.1080/02670836.2016.1153277
(37) Kong, L.; Cheng, B.; Wan, D.; Xue, Y. A Review on BCC-Structured High-Entropy Alloys for Hydrogen Storage. *Front. Mater.* **2023**, *10*, 1135864. https://doi.org/10.3389/fmats.2023.1135864

(38) Yang, X.; Zhang, Y. Prediction of High-Entropy Stabilized Solid-Solution in Multi-Component Alloys. *Mater. Chem. Phys.* **2012**, *132* (2), 233–238. https://doi.org/10.1016/j.matchemphys.2011.11.021
(39) Gao, Y.; Han, J.; Ge, F.; Zhang, X.; Cai, Y.; Cui, Y. Design of Eutectic High-Entropy Alloys in the Co-Cr-Ni-V-Ti-Al System Using Scheil Solidification Path Optimization. *J. Alloys Compd.* **2024**, *1002*, 175327. https://doi.org/10.1016/j.jallcom.2024.175327
(40) Amiri, A.; Shahbazian-Yassar, R. Recent Progress of High-Entropy Materials for Energy Storage and Conversion. *J. Mater. Chem. A* **2021**, *9* (2), 782–823. https://doi.org/10.1039/D0TA09578H
(41) Li, R.; Xie, L.; Wang, W. Y.; Liaw, P. K.; Zhang, Y. High-Throughput Calculations for High-Entropy Alloys: A Brief Review. *Front. Mater.* **2020**, *7*. https://doi.org/10.3389/fmats.2020.00290
(42) Ji, K.; Clarke, A. J.; McKeown, J. T.; Karma, A. Microstructure Development during Rapid Alloy Solidification. *MRS Bull.* **2024**, *49* (6), 556–567. https://doi.org/10.1557/s43577-024-00717-6
(43) Edalati, P.; Andrade, G.; Strozi, R. B.; Dangwal, S.; Edalati, K.; Floriano, R. Room Temperature Hydrogen Storage Properties of Ti-Zr-Mn-Fe-Co High-Entropy Alloys Designed by Semi-Empirical Descriptors, Thermodynamic Calculations and Machine Learning. *J. Alloys Compd.* **2025**, *1022*, 180051. https://doi.org/10.1016/j.jallcom.2025.180051
(44) Wu, H.; Zhang, D.; Yang, B.; Chen, C.; Li, Y.; Zhou, K.; Jiang, L.; Liu, R. Microstructural Evolution and Defect Formation in a Powder Metallurgy Nickel-Based Superalloy Processed by Selective Laser Melting. *J. Mater. Sci. Technol.* **2020**, *36*, 7–17. https://doi.org/10.1016/j.jmst.2019.08.007
(45) Gorsse, S.; Tancret, F. Current and Emerging Practices of CALPHAD toward the Development of High Entropy Alloys and Complex Concentrated Alloys. *J. Mater. Res.* **2018**, *33* (19), 2899–2923. https://doi.org/10.1557/jmr.2018.152
(46) Zhang, C.; Yang, Y. The CALPHAD Approach for HEAs: Challenges and Opportunities. *MRS Bull.* **2022**, *47* (2), 158–167. https://doi.org/10.1557/s43577-022-00284-8
(47) Zepon, G.; Silva, B. H.; Zlotea, C.; Botta, W. J.; Champion, Y. Thermodynamic Modelling of Hydrogen-Multicomponent Alloy Systems: Calculating Pressure-Composition-Temperature Diagrams. *Acta Mater.* **2021**, *215*, 117070. https://doi.org/10.1016/j.actamat.2021.117070
(48) Merlino, A. R.; Luna, C. R.; Juan, A.; Pronsato, M. E. A DFT Study of Hydrogen Storage in Zr(Cr 0.5 Ni 0.5) 2 Laves Phase. *Int. J. Hydrog. Energy* **2016**, *41* (4), 2700–2710. https://doi.org/10.1016/j.ijhydene.2015.10.077
(49) Zhu, Y.; Yang, X.-S.; Xu, Z.-L.; Tsui, G. C.-P.; Zhou, Q.; Tang, R.; Xiao, F.; Chan, K. Development of AB2-Type TiZrCrMnFeCoV Intermetallic High-Entropy Alloy for Reversible Room-Temperature Hydrogen Storage. *J. Energy Storage* **2024**, *75*, 109553. https://doi.org/10.1016/j.est.2023.109553
(50) Shen, X.; Zhou, G.; Liu, F.; Dong, F.; Zhang, Y.; Yuan, X.; Wang, B.; Luo, L.; Su, Y.; Cheng, J.; Liaw, P. K. Preparation of TiZrHfNbMo Refractory High Entropy Alloy Powder via Hydrogen Plasma-Arc Melting. *Intermetallics* **2024**, *173*, 108435. https://doi.org/10.1016/j.intermet.2024.108435
(51) Andrade, G.; Zepon, G.; Edalati, K.; Mohammadi, A.; Ma, Z.; Li, H.-W.; Floriano, R. Crystal Structure and Hydrogen Storage Properties of AB-Type TiZrNbCrFeNi High-Entropy Alloy. *Int. J. Hydrog. Energy* **2023**, *48* (36), 13555–13565. https://doi.org/10.1016/j.ijhydene.2022.12.134
(52) Khajavi, S.; Schlabach, S.; Pundt, A.; Huot, J. Oxidation and Compositional Modulation in Single Phase C14 Zr0.6Ti0.4Fe1Cr1 Alloy. *J. Alloys Compd. Commun.* **2024**, *3*, 100026. https://doi.org/10.1016/j.jacomc.2024.100026
(53) Fontana, G. L. B. G.; Edalati, P.; Dangwal, S.; Edalati, K.; Strozi, R. B.; Floriano, R. Crystal Structure and Hydrogen Storage Properties of ZrNbFeCo Medium-Entropy Alloy. *Intermetallics* **2025**, *176*, 108576. https://doi.org/10.1016/j.intermet.2024.108576

(54) Pan, Q.; Shen, H.; Han, X.; Zhu, J.; Li, Z.; Pan, T.; Xu, L.; Lv, L. Effect of Non-Stoichiometric Mn and Cr on the Hydrogen Storage Properties of Ti–Mn-Based Alloys. *RSC Adv.* **2025**, *15* (22), 17153–17163. https://doi.org/10.1039/D5RA00542F
(55) Payá, J.; Freni, A.; Corberán, J. M.; Compañ, V. Hydriding Kinetics of $LaNi_5$ Using Nucleation-Growth and Diffusion Models. *J. New Mater. Electrochem. Syst.* **2012**, *15* (4), 293–300. https://doi.org/10.14447/jnmes.v15i4.50
(56) Dangwal, S.; Ikeda, Y.; Grabowski, B.; Edalati, K. Machine Learning to Explore High-Entropy Alloys with Desired Enthalpy for Room-Temperature Hydrogen Storage: Prediction of Density Functional Theory and Experimental Data. *Chem. Eng. J.* **2024**, *493*, 152606. https://doi.org/10.1016/j.cej.2024.152606
(57) Dangwal, S.; Edalati, K. High-Entropy Alloy TiV2ZrCrMnFeNi for Hydrogen Storage at Room Temperature with Full Reversibility and Good Activation. *Scr. Mater.* **2024**, *238*, 115774. https://doi.org/10.1016/j.scriptamat.2023.115774
(58) Yin, F.; Chang, Y.; Si, T.; Chen, J.; Li, H.-W.; Li, Y.; Zhang, Q. Structural and Kinetic Adjustments of Zr-Based High-Entropy Alloys with Laves Phases by Substitution of Mg Element. *Energy Adv.* **2023**, *2* (9), 1409–1418. https://doi.org/10.1039/D3YA00243H
(59) Ma, X.; Ding, X.; Chen, R.; Cao, W.; Song, Q. Study on Hydrogen Storage Property of (ZrTiVFe) Al High-Entropy Alloys by Modifying Al Content. *Int. J. Hydrog. Energy* **2022**, *47* (13), 8409–8418. https://doi.org/10.1016/j.ijhydene.2021.12.172
(60) Ma, X.; Ding, X.; Chen, R.; Chen, X.; Song, Q.; Cui, H. Study on Microstructure and the Hydrogen Storage Behavior of a TiVZrNbFe High-Entropy Alloy. *Intermetallics* **2023**, *157*, 107885. https://doi.org/10.1016/j.intermet.2023.107885
(61) Dornheim, M. Thermodynamics of Metal Hydrides: Tailoring Reaction Enthalpies of Hydrogen Storage Materials. In *Thermodynamics - Interaction Studies - Solids, Liquids and Gases*; IntechOpen, 2011. https://doi.org/10.5772/21662
(62) El bahri, A.; Ez-Zahraouy, H. Enhancing Hydrogen Storage Properties of Titanium Hydride TiH2 with Vacancy Defects and Uniaxial Strain: A First-Principles Study. *Int. J. Hydrog. Energy* **2024**, *87*, 678–685. https://doi.org/10.1016/j.ijhydene.2024.09.065
(63) Kumar, A.; Yadav, T. P.; Shaz, M. A.; Mukhopadhyay, N. K. Hydrogen Storage Properties in Rapidly Solidified TiZrVCrNi High-entropy Alloys. *Energy Storage* **2024**, *6* (1), e532. https://doi.org/10.1002/est2.532
(64) Edalati, P.; Andrade, G.; Strozi, R. B.; Dangwal, S.; Edalati, K.; Floriano, R. Room Temperature Hydrogen Storage Properties of Ti-Zr-Mn-Fe-Co High-Entropy Alloys Designed by Semi-Empirical Descriptors, Thermodynamic Calculations and Machine Learning. *J. Alloys Compd.* **2025**, *1022*, 180051. https://doi.org/10.1016/j.jallcom.2025.180051
(65) Kumar, A.; Yadav, T. P.; Mukhopadhyay, N. K. Notable Hydrogen Storage in Ti–Zr–V–Cr–Ni High Entropy Alloy. *Int. J. Hydrog. Energy* **2022**, *47* (54), 22893–22900. https://doi.org/10.1016/j.ijhydene.2022.05.107



Journal Pre-proof

Declaration of interests

☒The authors declare that they have no known competing financial interests or personal relationships that could have appeared to influence the work reported in this paper.

☐The authors declare the following financial interests/personal relationships which may be considered as potential competing interests:

Journal Pre-proof

- Non-equiatomic alloy was rationally designed by combining semiempirical parameters with computational thermodynamic tools.
- Volumetric PCT measurements show a maximum hydrogen capacity of 1.56 wt% ($H/M = 1.08$) at 70 °C under 10 MPa.
- The alloy exhibits extremely fast kinetics with no incubation time and reversible storage at moderate temperatures.

Journal Pre-proof